Revision 2 Manuscript #5690:

Structural incorporation of W^{6+} into hematite and goethite: a combined study of natural and synthetic iron oxides developed from precursor ferrihydrite

Stefan Kreißl [*a], Ralph Bolanz [b], Jörg Göttlicher [c], Ralph Steininger [c], Mihail Tarassov [d], Gregor Markl [a]

[*] corresponding autor; e-mail: stefan.kreissl@uni-tuebingen.de; phone: +49 70712973166

[a] Eberhard Karls University, Faculty of Science, Department of Geosciences, Petrology and Mineral Raw Materials, Wilhelmstraße 56, 72074 Tübingen, Germany

[b] Friedrich Schiller University, Institute of Geosciences, Department Mineralogy and Geochemistry, General and Applied Mineralogy, Carl-Zeiss-Promenade 10, 07745 Jena, Germany

[c] Karlsruhe Institute of Technology, ANKA Synchrotron Radiation Facility, Hard X-ray Spectroscopy, Hermann-von-Helmholtz-Platz 1, 76344 Eggenstein-Leopoldshafen, Germany

[d] Bulgarian Academy of Sciences, Institute of Mineralogy and Crystallography, Department Mineralogy and Mineral Raw Materials, Acad. Georgi Bonchev Str., bl. 107, 1113 Sofia, Bulgaria

E-mail list:

Stefan Kreißl: stefan.kreissl@uni-tuebingen.de

Ralph Bolanz: ralph.bolanz@uni-jena.de

Jörg Göttlicher: joerg.goettlicher@kit.edu

Ralph Steininger: ralph.steininger@kit.edu

Mihail Tarassov: mptarass@dir.bg

Gregor Markl: gregor.markl@uni-tuebingen.de

Abstract

Hematite (α-Fe_2O_3) and goethite (α-FeOOH) can incorporate considerable amounts of tungsten. Although tungsten concentrations up to several wt% in hematite and goethite have been reported in the literature, none of the proposed models for a structural incorporation has been generally accepted yet. Here, the first combination of X-ray absorption fine structure (XAFS) measurements with X-ray diffraction (XRD), Raman spectroscopy (RS), electron microprobe (EMPA) and total reflection X-ray fluorescence (TXRF) provides a general relation between W content and its structural incorporation into hematite and goethite.

Botryoidal specimens of goethite and hematite, obtained from the Schwarzwald ore district, Black Forest, SW Germany and from the Grantcharitza tungsten deposit, Bulgaria, display W concentrations of up to 5.5 and 2.15 mol% W for goethite and hematite, respectively. In addition to these natural specimens, goethite and hematite were synthesized in the presence of W and incorporate up to 7 and 1.3 mol% W, respectively.

X-ray diffraction analysis does not indicate the presence of separate W-phases, supporting the structural incorporation of W into the hematite and goethite. Refined unit cell parameters indicate no changes with increasing W concentration in the hematites' but a rising structural disorder within the structure of the synthetic goethites. Raman spectroscopy, however, shows an increasing structural disorder for both synthetics, indicating an increase of Fe vacancies in both hematite and goethite. A deprotonation mechanism for the goethite structure is unlikely according to the Raman results.

XAS near edge spectra indicate a strong distortion of the WO_6 octahedra in both hematite and goethite. Extended XAFS spectra of the natural and synthetic goethites and hematites show

striking similarities and suggest that W^{6+} resides in all samples on the Fe^{3+} position, again without developing separate tungsten phases.

Calculations of the Fe-loss related to W incorporation reach mean values of ~2.9 and ~2.8 for goethite and hematite, respectively. The formation of two Fe^{3+}-vacancies in close proximity to the newly incorporated W^{6+} in addition to a protonation of the structures achieves charge balance within the hematite and goethite structure.

Hematite and goethite record the presence of W in fluids even in the absence of visible W minerals. After W adsorption to ferrihydrite (the hematite and goethite precursor phase) and after its transformation to either hematite or goethite, only hematite with up to 0.4 wt.% W is clearly able to continuously monitor a changing W signature as a record of the fluid history within its oscillatory growth zones. In contrast, goethite is probably not a good monitor of a primary W fluid history. Their combination, however, could be particularly useful, as hematite records the W concentrations in a fluid during ferihydrite precipitation, while goethite records W concentrations during later ferrihydrite maturation. Botryoidal Fe-ores have never been considered for W recovery but could play an important role to fight a potential supply risk of W as a high-technology metal.

Keywords: tungsten, iron oxides, iron hydroxides, substitution, hydrothermal, crystallography, spectroscopy, XAFS

Introduction

Tungsten is a vital metal for our modern industry and is used in many modern applications reaching from high-temperature and mechanically resistant electrodes, as an additive in metal alloys for high-temperature resistant steel to cathodes for microwave magnetrons and as substitute for lead and uranium in specific ammunition types (Koutsospyros et al. 2006). In 2010, the European Union rated W as a critical resource due to its economic importance and foreseeable supply risk (EU Commission 2010). In addition to its economic value, tungsten variations in oscillatory zonation patterns of katathermal garnets, were used to interpret the chemical evolution of hydrothermal systems by recording distinct fluid batches (Jamtveit et al. 1993).

Besides the most important W ore minerals, wolframite ($(Fe,Mn)WO_4$) and scheelite ($CaWO_4$), iron oxides formed under hypogene and supergene conditions can exhibit high concentrations of W with up to ~0.5 mol% (hypogene; Benvenuti et al. 2013) and 5.5 mol% (supergene; Tarassov et al. 2002). Hematite and goethite are suitable candidates to be investigated for fluid evolution studies, because they show an intense oscillatory zonation of W, which is essential for such studies (cf. e.g. Haase et al. 1980; Manning and Bird 1990; Jamtveit 1991; Yardley et al. 1991; Putnis et al. 1992; Jamtveit and Hervig 1994; Jamtveit et al. 1993, 1995).

At low temperatures and under near-surface conditions, hematite and goethite are both transformation products of ferrihydrite ($Fe_{10}^{3+}O_{14}(OH)_2$; Michel et al. 2007), a poorly crystalline ferric oxide, which forms during the early stages of Fe^{2+} oxidation, its hydrolysis and a rapid supply of Fe-monomers and -dimers (Cornell and Schwertmann 2003). Jambor and Dutrizac (1998) and references therein summarize structural observations, the transformation of ferrihydrite to hematite and goethite and its composition. During the formation of ferrihydrite,

other chemical elements such as W become immobilized in significant quantities, either by surface adsorption or by co-precipitation (Kashiwabara et al. 2013). Depending on temperature, pH, and the presence of other ions, ferrihydrite then transforms to goethite (via a dissolution-reprecipitation process) or to hematite (by a topotactic solid-state transformation; Cornell and Schwertmann 2003; Cudennec and Lecerf 2006). These two formation mechanisms are highly significant for the structural incorporation of minor elements into hematite and goethite, since W-bearing hematite forms from W-bearing ferrihydrite, while W-bearing goethite forms during the polymerization of it's $Fe^{3+}O_6$-octahedra in W enriched solutions.

Hence, for the structural incorporation of W into hematite and goethite, the structural characteristics of both phases are of great importance. The structures of goethite and hematite consist of hexagonal close packing (hcp) arrays of anions (O_2^- and OH^- for goethite and O_2^- for hematite) stacked along the [001] direction with Fe^{3+} ions occupying 1/2 (for goethite) and 2/3 (for hematite) of the octahedral sites. Goethite is isostructural with diaspore (α-AlOOH) and consists of FeO_6 double chains oriented parallel to [010]. The edge-sharing FeO_6-octahedra form double chains connected by corner-sharing among each other (Alvarez et al. 2008). Hematite, on the other hand, is isostructural with corundum. The FeO_6-octahedra in hematite are connected by corner-, edge-, and face-sharing which results in significantly shorter Fe-Fe distances for the face-sharing FeO_6-octahedra.

For a successful substitution of Fe^{3+}, W^{6+} has to be octahedrally coordinated by oxygen. At pH >4.4, tungsten is predominantly present as dissociated, tetrahedral coordinated WO_4^{2-}. At pH <4.4, W occurs as $WO_3(H_2O)_3$ in octahedral coordination (Cruywagen 2000; Smith et al. 2001). Kashiwabara et al. (2013) showed that W adsorbs as distorted, octahedral coordinated inner-sphere surface complex on ferrihydrite, goethite and hematite

Besides the structural characteristics of the host phases, the strong Jahn-Teller distortion of the WO_6-octahedron (Hsin et al. 2008) may also affect the structural incorporation of W^{6+}. For example, in the tungstite structure, the highly asymmetric WO_6-octahedron displays one short W=O bond of 1.69 Å, four intermediate W-O bonds with 1.83 Å and 1.93 Å, as well as one long bond distance of 2.34 Å (Szymański and Roberts 1984).

Although homovalent substitutions of Fe^{3+} by trivalent ions were extensively investigated (cf. summary in Cornell and Schwertmann 2003), heterovalent substitutions like $Fe^{3+} \rightarrow W^{6+}$ received significantly less attention (e.g. Sieber et al. 1985; Duff et al. 2002; Scheinost et al. 2006; Nico et al. 2009; Mitsunobu et al. 2010; Bolanz et al. 2013a, 2013b; Marshall et al. 2014; Brinza et al. 2015). The structural incorporation of W^{6+} into hematite and goethite by heterovalent substitution ($2\ Fe^{3+} \rightarrow W^{6+} + \square^{0}$) has already been proposed in previous investigations, the exact modes of incorporation, however, were never investigated by close-range order techniques like EXAFS (Kolitsch 1998; Tarassov et al. 2002; Ciobanu et al. 2013). In addition, it was not conclusively shown that W is part of the hematite and goethite crystal structure and not only present as microinclusions of a different phase or adsorbed to the iron oxide surface. This question of structural incorporation vs. adsorption is particularly important, as adsorbed ions can easily be released by a slight change in pH, while structurally bound elements are immobilized on the long-term. Therefore, in order to decipher the history of a fluid by fluctuations in W content, detailed information about the speciation of W^{6+} in iron oxides is essential and will be addressed in this study.

By using a combination of chemical and spectroscopic techniques, the potential substitution of Fe^{3+} by W^{6+} and the exchange and charge balance reactions for this substitution within the hematite and goethite structure will be discussed.

Samples

Natural specimens of tungsten-rich botryoidal hematite and goethite were obtained from various iron ore deposits from the Schwarzwald ore district, Germany and the Grantcharitza tungsten ore deposit, Bulgaria. Samples originating from the Schwarzwald are mostly uncorrelated to W-mineralization and were denoted with the abbreviation BF (Black Forest = english for Schwarzwald). Samples from Grantcharitza come from the weathering zone of a W-deposit and are denoted with GR. The investigation of these natural specimens is complemented by an investigation of precisely synthesized iron oxides with the denotation SYN. For all synthesized samples and hematite from sample BF-26, powdered specimens with different W-concentrations were prepared to correlate refined lattice parameters and their chemistry (cf. Table 1). In the natural samples of the GR deposit and in BF-26, hematite and goethite occur intimately intergrown with each other, while the sample BF-11 consists of hematite and BF-20 of goethite exclusively (cf. Table 2).

Although different physicochemical conditions prevailed during their formation, textural features of all natural samples and the method of the synthesis suggest that all hematite and goethite samples developed from ferrihydrite as precursor phase

The natural samples represent secondary assemblages of primary Fe- or W-mineralizations. Tarassov et al. (2002) already described the GR samples; text and Fig. B1 in Appendix B1 describe the BF samples and include information about the formation ages, tectonic settings, primary mineral assemblage, and linkage to minor W-mineralizations of both the GR and BF samples.

Methods

Synthesis of W-bearing hematite and goethite (SYN samples)

The precursor for all synthetic W-hematite samples was two-line ferrihydrite ($Fe_{10}^{3+}O_{14}(OH)_2$; Michel et al. 2007), synthesized according to Schwertmann and Cornell (2000). Appendix B2 reports the preparation of suspended ferrihydrite used for the synthesis of hematite (pH 4) and goethite (pH 12). For W-bearing goethite and hematite, the respective suspensions were spiked with different concentrations of sodium tungstate (Na_2WO_4), calculated to arrive at molar W/Fe ratios of 0, 0.05, 0.1, 0.2, 0.4, 0.8, and 1.6.

Subsequently, samples for hematite synthesis were filtered and washed with 500 mL of deionized water, air-dried, and heated in an oven for 72 h at 500 °C. After the transformation of ferrihydrite to hematite, the samples were finely ground and washed for about 15 minutes with HCl (15 %) in order to remove remaining ferrihydrite. Afterwards, the hematite samples were washed with deionized water for HCl removal, filtrated, air-dried, and sealed in glass vials.

For the synthesis of W-bearing goethite, the ferrihydrite slurry was split into two equal portions, the volume of the slurry was adjusted to 250 mL each, and filled in 250 mL polyethylene bottles. One aliquot was aged in an oven at 70 °C for 60 days, whereas the other was aged at 25 °C for the same time. In order to remove remaining ferrihydrite, all goethite samples were washed with 250 mL of a 0.2 M ammonium oxalate ($(NH_4)_2C_2O_4$) solution with a pH of 3 (Schwertmann 1964). The pH of the ammonium oxalate solution was adjusted with a 1 M HNO_3. After the ferrihydrite extraction, all samples were rinsed with deionized water, filtrated, air-dried, and sealed in glass vials. Denotations, corresponding to the initial molar W/Fe ratios, are SYN-hem$_{0.00}$ to SYN-hem$_{1.6}$ for the hematite samples, SYN-goe$_{0.00;25°C}$ to SYN-goe$_{1.6;25°C}$ of the goethite samples aged at 25 °C and SYN-goe$_{0.00;70°C}$ to SYN-goe$_{1.6;70°C}$ for samples aged at 70 °C accordingly.

Electron microprobe analysis (EMPA)

Elemental composition of the natural and synthetic samples was determined using a JEOL JXA-8900RL electron microprobe in wavelength-dispersive mode at the Fachbereich Geowissenschaften of the University of Tübingen, Germany; quantitative element distribution maps of W were additionally obtained on a JEOL JXA-8230 at the Institute of Geosciences, Friedrich-Schiller-University Jena, Germany. Natural and synthetic standards were used for calibration, the exact specifications can be found in Table A1 of Appendix A. For focused beam measurements, a beam current of 20 nA and an acceleration voltage of 20 kV were used. For element maps, a beam current of 50 nA, an acceleration voltage of 20 kV, and a dwell time of 300 ms/pixel were used to reach comparable count rates.

Although most samples showed no problems during the WDX analyses, the synthetic iron oxides showed low totals due to their high porosity. The chemical composition of all synthetic samples was therefore additionally investigated by total reflection X-ray fluorescence spectrometry (TXRF) (see below).

Table 1 shows the EMPA data of the synthetic and natural powder samples, which were also used for refinement of crystallographic parameters; Table 2 shows the EMPA data of the natural hematite and goethite samples BF and GR, respectively.

Total reflection X-ray fluorescence (TXRF)

Concentrations of W and Fe in the synthetic samples and the natural sample BF-26 were additionally analyzed by total reflection X-ray fluorescence using a TXRF Bruker S2 PICOFOX at the Fachbereich Geowissenschaften of the University of Tübingen, Germany, equipped with a Mo-anode operating at 50 kV and 600 µA. This method was chosen to confirm the EMPA analyses of the porous samples. To compare refined crystallographic parameters with the W-

concentrations of the respective samples, the same samples were also used for powder X-ray diffraction measurements (next chapter).

Parts of the natural hematite sample BF-26 showing different W concentrations with EMPA were measured as solids to avoid undesired precipitates during chemical extraction. About 2 mg of powdered sample and 20 µL of a 100 µg/g Sr-solution as internal standard were dispersed with 1 mL Triton X-100 solution and dried for 5 min at 70 °C on quartz discs. The reliability of this method has been shown by Cantaluppi et al. (2013). For each zone three aliquots were prepared and analyzed with a measurement time of 300 s, respectively. The observed data of the different zones are listed and compared to refined lattice parameters in Table 1.

According to the initial W/Fe molar solution ratios during the iron oxide synthesis, about 1-20 mg powder was digested in 15 mL HCl (32%) and 10 mL MilliQ water to reach comparable count rates, respectively. At these low W concentrations in HCl solution, no precipitation was observed. To determine the W-concentration, 450 µL of the undiluted sample solutions were mixed with 50 µL of a 5 µg/g Ga-solution as internal standard. For Fe determination the sample solutions were diluted 1:10 with MilliQ water to the chloride concentration (Stosnach, 2010), which could cause coagulation of crystallites, resulting in additional disturbing background effects (De La Calle et al., 2013). A volume of 400 µL of these diluted solutions were mixed with 100 µL of a 100 µg/g Ga-solution as internal standard. All solutions were dried for 5 min at 70 °C on quartz discs and measured for 600 s each. The spectra were evaluated with the Bruker Spectra 6.2.0.0 software.

For all synthetic W-bearing samples, the molar loss of Fe for each mole of W can be calculated using Eq. 1:

$$\text{Eq. 1: } \frac{Fe-loss}{W} = \frac{(Fe_{wt\%}^{W_0} - Fe_{wt\%}^{W_X}) \cdot M_W}{W_{wt\%}^{W_X} \cdot M_{Fe}}$$

where $Fe_{wt\%}^{W_0}$ is the Fe content of the W-free goethite or hematite, $Fe_{wt\%}^{W_X}$ is the Fe content of W-bearing goethite or hematite, M_W and M_{Fe} are the molecular weights of W and Fe and $W_{wt\%}^{W_X}$ is the W content of W-bearing goethite or hematite. All Fe and W concentrations need to be corrected for the measurement total. The obtained chemical data of the synthetics are listed and compared to the Fe-loss and refined lattice parameters in Table 1.

For comparing the W concentrations between hematite/goethite and between synthetic/natural samples, the molar fraction of W in hematite and goethite $x_W^{hematite\,/\,goethite}$ was calculated using Eq. 2:

$$\text{Eq. 2: } x_W^{hematite\,/\,goethite} = \left(\frac{n_W}{n_W + \sum n_i} \right)_{hematite\,/\,goethite}$$

where n_W stands for the moles of W and Σn_i for the sum of moles of all other elements present within hematite or goethite. For the synthetic samples, Σn_i corresponds to Fe only, for the natural samples to the elements incorporated besides W according to Table 2.

Powder X-ray diffraction (pXRD)

For phase identification and crystallographic parameters, powder X-ray diffraction (pXRD) patterns of all synthetic samples, the natural sample BF-26, and the reference compounds were collected with a Bruker D8 AXS Advance diffractometer with Cu Kα radiation (λ = 1.54058 Å) at the Friedrich-Schiller-University Jena, Germany. The patterns were collected at 20 °C between 5-130 °2θ with a step size of 0.02 °2θ and a dwell time of 1 second. For refinement, the patterns of all samples were processed with the program TOPAS®, where a fitting range between 15-130 °2θ was chosen. For each fit, the statistical measures from the obtained data are given including

the residuals for the weighted profile (R_{wp}) and the goodness-of-fit (GOF) (see Table 1). For sample BF-26, predefined regions of the botryoidal hematite, previously investigated by EMPA, were ground in an agate mortar (cf. Table 1; sample aliquots BF-26 I-VII). However, due to the small sample size and volume, all other goethite samples had to be analyzed by micro X-ray diffraction (see next chapter).

Micro-resolved X-ray diffraction (µXRD)

Due to dilution effects during the preparation of the natural powder samples, resulting in low W contents, additional micro X-ray diffraction analyses were performed in regions of the thin sections with the highest W concentrations to exclude a potential intergrowth of discrete W-bearing impurities. For the regions of interest, the spots with maximum W concentration, previously determined by EMPA, were chosen. All µXRD measurements were performed on thin sections of sample BF-11, BF-20, and BF-26 with a Bruker D8 Discover GADDS theta-theta micro-diffractometer at the Fachbereich Geowissenschaften, Universität Tübingen, Germany. To prevent iron fluorescence, a Co-anode with Kα radiation (λ = 1.79 Å) was used at 30 kV and 30 mA with a HOPG monochromator and monocapilarry optics of 500 µm with a 200 µm pinhole. The incident angle to the samples was fixed to 10°. For the general area detector diffraction system (GADDS) a Bruker VÅNTEC500 detector was used and the patterns were integrated between 5-68 °2Θ. Selected µXRD-patterns can be found in Fig. A1 of Appendix A.

Micro-Raman spectroscopy (µRS)

µRS was preformed to determine the purity of the natural and synthetic hematite/goethite samples as well as to identify the possible effects of the structural incorporation of W on the vibrational modes of both phases. In addition, µRS was used to distinguish between the two possible charge balance mechanisms, Fe^{3+}-vacancy formation or oxygen (de)protonation by H^{+}.

For the measurements, a confocal Raman spectrometer Renishaw InVia Reflex with a laser wavelength of 532 nm was used at the Fachbereich Geowissenschaften of the University of Tübingen, Germany. A laser power of ~0.2 mW at the sample surface was used to avoid thermal degradation of the samples. The significant part of the recorded Raman spectra were characterized by strong fluorescence signals. Therefore, the recorded spectra were baseline corrected by polynomial and linear fits for full spectra and detail spectra, respectively. Mixed Gaussian and Lorentzian curves were used for the deconvolution of the peak fits. Measurements, baseline subtraction and peak fits performed by using the Renishaw software package WiRE 3.0.

X-ray absorption near edge structure (XANES) spectroscopy

X-ray absorption near edge (XANES) spectra were measured at the W L_1 and L_3 edges at the SUL-X beamline of the Angströmquelle Karlsruhe (ANKA, Karslruhe, Germany) using a fixed exit double crystal monochromator. W L_3 edge XANES spectra were additionally recorded for the natural hematite sample BF-26 using the Si(311) monochromator crystal pair or decreasing of the slit 4 (intermediate focus) width at Si(111) monochromator crystals to investigate the effect of energy resolution of spectral features (for details see Appendix B3). Additionally, XANES spectra at the Fe K-edge were measured using the Si(111) monochromator crystal pair.

Beam sizes for XANES measurements on the thin sections were about 100 µm x 100 µm at sample position to ensure data recording of the area of interest. Only for the tests with higher energy resolution using the Si(111) monochromator crystals, a smaller beam size of 50 µm x 50 µm was required.

W L_3- and Fe *K*-edge spectra were measured on natural and synthetic powder samples (BF-26, BF-20, SYN-goe$_{0.05;25°C}$, SYN-goe$_{0.05;70°C}$, SYN-goe$_{1.6;70°C}$, SYN-hem$_{0.05}$ and SYN-hem$_{1.6}$) in transmission and fluorescence mode on cellulose pellets and in fluorescence mode only on the

thin sections (BF-26 and BF-20). W L_1–edge spectra were measured except for W-rich hematite BF-26 and (due to low W concentration in natural goethites) for the synthetic sample $SYN_{goe0.05;70°C}$ (cf. Appendix B3).

Reference spectra at the W L_3 and W L_1 edge were measured for $Na_2WO_4 \cdot 2H_2O$ and $CaWO_4$ (scheelite) representing W in tetrahedral O coordination as well as $(Fe,Mn)WO_4$ (wolframite) and $MnWO_4$ (hübnerite) where W^{6+} is in octahedral coordination.

Energy calibrations, pre- and post-edge background corrections of W L_3, W L_1 and Fe K spectra, the used transmission and fluorescence methods, energy resolution, self absorption correction of the Fe K spectra as well as the extraction of the W L_3-edge spectra energy gap and the W L1 pre-edge area to identify WO_6 octahedra distortions after Yamazoe et al. (2008) are reported in Appendix B3.

Extended X-ray absorption fine-structure (EXAFS) spectroscopy

For all natural and synthetic samples, extended X-ray absorption fine-structure (EXAFS) spectra were collected at the W L_3 edge at the SUL-X beamline of the Angströmquelle Karlsruhe (ANKA, Karlsruhe, Germany) using a Si(111) crystal pair with a fixed beam exit as monochromator. The appropriate mass of each sample and reference compound, calculated with the program XAFSmass (Klementiev 2012), was mixed with cellulose powder, homogenized, and pressed to a pellet. Measurement parameters of the EXAFS region are presented in Appendix B3. The spectra were used for the EXAFS evaluation up to 12.8k (640.8 eV above the absorption edge).

Samples measured as thin sections were collected in fluorescence mode, whereas all samples and reference compounds prepared as pellets were additionally measured in transmission mode (cf. chapter above). Depending on the quality of the measurement, either the fluorescence or transmission signal was chosen.

All EXAFS data were processed and fit by the Athena and Artemis software package (Ravel and Newville 2005). In order to reduce the noise in higher k-range, the spectra of all synthetic goethite samples were merged and denoted SYN-goe$_{0.05\text{-}1.6;70°C}$. Equally, all spectra of synthetic hematite were merged and denoted SYN-hem$_{0.05\text{-}1.6}$.The paths, generated for the fitting, were calculated from modified models of hematite (Blake et al. 1966) and goethite (Gualtieri and Venturelli 1999) for all paths. The paths were generated using the software program FEFF6 (de Leon et al. 1991), embedded in the Artemis software package.

For each EXAFS fit, the statistical measures of the deviation of the fit from the obtained data are given, including the number of variables allowed to float in the fit (N_{var}), the number of independent data points (N_{idp}), as well as the R-factor. The N_{idp} is equal to $2\Delta kR/\pi$ where k and R are the fitting ranges. The R factor is defined by Eq. 3,

$$\text{Eq. 3: } R = \frac{\sum\left(\chi_i^{data} - \chi_i^{model}(x)\right)^2}{\sum\left(\chi_i^{data}\right)^2}$$

where χ is the magnitude of the EXAFS oscillations and x is the set of variables to be refined. EXAFS spectra of the individual reference compounds were fit with the respective structures in order to identify problems that could be encountered when fitting the model of the structurally unknown samples. Additional information about the fitting procedure can be found in Appendix B5.

Results

Homogeneity and purity of the natural samples

Botryoidal hematites and goethites show a high porosity (see Fig. 1a, c and e). Thus, distinct W-phases could have formed after iron mineral formation, due to later W-rich fluid infiltration. To avoid any possible misinterpretation of our data, the absence of distinct W-phases, the homogeneity and purity of the natural samples was tested by EMPA element distribution maps, 2D-resolved µXRD and µRS on regions with the highest W concentrations of the BF samples.

The results of the µXRD for the BF samples did not show any other diffraction reflexes besides those of hematite or goethite at their highest W concentrations of 1.1-1.8 wt% and 0.3 wt%, respectively (Fig. A1). µRS of the same spots show bands very similar to those observed for pure, synthesized α-Fe_2O_3 and α-FeOOH by De Faria et al. (1997) and Bersani et al. (1999). Only the synthetic goethites show an additional band at 417 cm^{-1}, which has not been published for goethite yet (see chapter below).

The EMPA element distribution maps show, that W is generally homogeneously distributed (Fig. 1). The count rates of the W*L*α fluorescence (Fig. 1; right side) do not show any correlation to the lowest count rates of the back-scatter electron (BSE) images (Fig 1; left side), which are decisive for the porosity and interstitial space between the single crystallites. In general, the W*L*α fluorescence maps indicate no abnormal W-rich clusters, which would indicate a separate W phase. Only Fig. 1b and d show rhythmic variations of the W*L*α fluorescence, which can be attributed to different W concentrations within the iron oxides during separate growth stages. E.g. initial, globular aggregates in Fig. 1a and b show much higher W concentrations (green colors; up to ~1.24 wt% W) than the following feather-like aggregates (blue colors; ≤0.2 wt% W).

The samples from Grantsharitza ($GR_{G-I,G-II,H-I}$) were already analyzed for phase purity in Tarassov et al. (2002), showing hematite, goethite, quartz and microcline reflexes only (their Fig. 1). The measurement of a W-rich phase F_W (cf. Appendix B1), microscopically not identified as hematite or goethite with concentrations of up to ~20±0.26 wt% W was avoided during the XAFS measurements.

Chemistry of the natural and synthetic W-rich hematites and goethites

The W- and Fe-composition of the powdered synthetic samples and BF-26, quantified by TXRF and EMPA is shown in Table 1. Additionally, the amount of Fe loss for each incorporated W is given for the synthetic samples. Representative chemical compositions of all natural samples, obtained by EMPA are shown in Table 2.

In general, hematite samples from the Schwarzwald exhibit significantly higher concentrations of W compared to their goethite counterparts (Fig. 2b). Hematite (BF-26), completely unrelated to any W-mineralization, exhibits the highest W concentration with 2.16 wt% WO_3 (0.8 mol% W), whereas hematite sample BF-11, correlated with scheelite mineralization, shows only a maximum of 1.61 wt% WO_3 (0.6 mol% W). However, goethite samples from the Schwarzwald exhibit only low W contents with a maximum of 0.33 wt% WO_3 (0.12 mol% W) in sample BF-20.

In contrast, the samples from the Grantcharitza tungsten deposit exhibit their highest concentrations in goethite with WO_3 up to 13 wt% (5.5 mol% W) in sample GR_{G-I} and 5.6 wt% (2.15 mol% W) in hematite GR_{H-I} (Fig. 2b). The synthetic W-doped samples also show higher W concentrations in goethite compared to hematite, reaching maximum WO_3 of about 8.9 wt% (7 mol% W) in goethite and 3.0 wt% (1.2 mol% W) in hematite (Fig. 2a).

According to Fig. 2a, TXRF and EMPA, show comparable values of W only at molar W/Fe ratios ≤ 0.1 within the synthesis solution. The synthetics, which precipitated at higher W/Fe ratios

show considerable variations between the TXRF and EMPA methods, whereas hematite shows a higher scatter of the EMPA data. Except for samples SYN-goe$_{0.1;70°C}$ and SYN-goe$_{1.6;70°C}$, the TXRF data show a general underestimation with respect to the EMPA mean values. Excluding sample SYN-goe$_{0.2;70°C}$ and SYN-hem$_{1.6}$, TXRF and EMPA represent overlapping values in case of the TXRF analysis relative error and the variability of the EMPA measurements (Fig. 2a, grey shaded areas).

Besides these deviations, however, the mean EMPA values of W in hematite and goethite indicate a linear increase with respect to initially low W concentrations used during the synthesis (Fig. 2a, dotted lines). For both, hematite and goethite, this linearity deviates from the observed data with a further increase of W in the synthesis solution. For goethite, the trend changes to a flatter slope, but continues as a different linear correlation. In contrast, hematite shows an abruptly higher spread with the increase of W in the synthesis fluids at molar W/Fe-ratios ≥ 0.2. These different changes occur earlier for goethite (~25 mmol/L W) than for hematite (~40 mmol/L W), and only concentrations in hematite display a plateau at ~1.2 $X_W^{hematite}$ (Fig. 2a). The goethite sample SYN-goe$_{0.4;70°C}$ shows a much higher W concentration than the illustrated linearity by both EMPA and TXRF, the hematite sample SYN-hem$_{1.6}$ is under-determined only by TXRF. According to the Fe-loss calculations (see Table 1), each W atom replaces ~2.9 Fe atoms of the goethite and ~2.8 of the hematite structure.

Powder X-ray diffraction

Powder X-ray diffraction patterns of the synthetic samples and sample BF-26 only display reflections characteristic of hematite or goethite, respectively. The refined lattice parameters and crystallite sizes of the full-profile fits are given in Table 1. It seems obvious that the lattice parameters do not correlate with the W concentrations for hematite samples (SYN-hem). However, in the synthetic goethites (SYN-goe), the unit cell parameter *c* and their crystallite sizes

correlate with their W content. With rising W concentration the unit cell parameter c increases as well as the crystallite size (cf. Fig. A2). Goethite SYN-goe$_{0.4;70°C}$, grown from solution, does not follow this trend as well as sample hematite SYN-hem$_{1.6}$, which shows a crystallite size about 1.5 times higher than the others. These deviations also coincide with their chemistry (cf. section above).

X-ray absorption near-edge spectroscopy

XANES at the W L_3 edge. The normalized, W L_3 μXANES spectra of the natural, W-rich goethite BF-20 and hematite BF-26, as well as two synthetic goethites (SYN-goe$_{0.05;25°C}$, SYN-goe$_{0.05;70°C}$) and synthetic hematite (SYN-hem$_{0.05}$) are shown in Fig. 3. The whiteline of the goethite BF-20 spectrum is slightly smaller than the one of hematite BF-26. Similar is valid for the spectra of the synthetic samples: The whiteline of goethite SYN-goe$_{0.05;25°C}$ is smaller than the one of hematite (SYN-hem$_{0.5}$) whereas the whiteline width of goethite SYN-goe$_{0.05;70°C}$ is close to the one of hematite. A better energy resolved spectrum is additionally shown for the natural hematite BF-26 (Fig. 3, dotted line of spectra a) and demonstrates the composite nature of the whiteline consisting of two individual peaks respectively at ~10211.7 eV and 10215 eV. Spectra with higher energy resolution have not been measured for other samples because the low flux conditions for higher energy resolution measurements were contrary to the beam requirements for collection EXAFS data of good signal to noise ratio. The hematites, the natural goethite BF-20 and the synthetic goethite SYN-goe$_{0.05;70°C}$ show an asymmetric whiteline with lowering of its intensity at the higher energy flank. The widths of all whitelines of the sample spectra are unambiguously broader and less sharp than those of the reference compounds $CaWO_4$ and $Na_2WO_4{\cdot}2H_2O$ (Fig. 3) where W has a tetrahedral coordination. The whitelines shapes of the octahedral coordinated W references $MnWO_4$ and $(Fe,Mn)WO_4$ (Fig. 3) are matching better with

those of hematite and goethite but asymmetry is absent or weak. The double whiteline features in $MnWO_4$ and $(Fe,Mn)WO_4$ are not visible because they were measured with Si(111) monochromator crystal pair and wide slit gaps. However, the split character of the W L_3 whiteline has besides the peak deconvolution been proved by the double peak structure of the second derivatives of the XANES spectra (Fig. A3). Crystal orientation effects, as the origin of different whiteline shapes, have been excluded because spectra measured on material from BF-20 goethite and BF-26 hematite areas, separated, grinded and pressed to cellulose pellets (resulting in randomly oriented crystals). They show the same spectral features as described for the measurements on the polished sections in Fig. 3 where crystallites show a common orientation (Fig. 1c and e). Appendix B4 and Fig. A4.1 report results of the W L_3 whiteline split quantification by peak deconvolution of selected samples and reference compounds.

XANES at the W L_1 edge. Natural hematite (BF-26) and the synthetic W containing goethite (SYN-goe$_{0.05;70°C}$) has been measured. Sample spectra are compared to the reference compounds $CaWO_4$, $Na_2WO_4{\cdot}2H_2O$, $MnWO_4$ and $(Fe,Mn)WO_4$ in Fig. 4. Both W L_1 XANES spectra of hematite BF-26 and goethite SYN-goe$_{0.05;70°C}$ are similar and show a double peak shaped XANES region besides the pre-edge. Both pre-edge peaks are located at ~12107.3 eV. The overall spectral shapes of the sample spectra are closest, among the reference spectra of this study, to hübnerite ($MnWO_4$) and wolframite ($(Fe,Mn)WO_4$) that represent W in octahedral coordination. The pre-edge peak for goethite is more distinctive than for hematite. The tetrahedral coordinated W of the references $CaWO_4$ and $Na_2WO_4{\cdot}2H_2O$ show well developed and high intensity pre-edge peaks at ~12105.1 eV (Fig. 4). Fits of the pre-edge peaks are shown in Fig. A4.2. The XANES region of the sample spectra is characterized by a double peak structure whereas spectra of the reference substances show three peaks well visible for $CaWO_4$ and

$Na_2WO_4 \cdot 2H_2O$ and less pronounced for the wolframite and hübnerite spectra. Peaks of the reference spectra are assigned with A (pre-edge) and B, C, D for the XANES region (Fig. 4).

XANES at the Fe K edge. After self absorption correction the Fe K XANES spectra of natural goethite (BF-20) and hematite (BF-11) measured on thin sections are compared to a goethite and hematite reference spectra (Fig. A5.1 and A5.2). The spectrum of goethite BF-20 matches well with the goethite reference spectrum, the one of hematite BF-11 with the hematite reference.

Extended X-ray absorption fine structure spectroscopy at the W L_3 edge

EXAFS measurements were performed for detailed information about the local environment of W^{6+} in W-bearing goethite and hematite. All Fourier-transformed EXAFS spectra of W-bearing goethite and hematite are shown in Fig. 5a and 5b, respectively. Appendix B5 summarizes the fitting procedure used for the W-O and W-Fe paths for both phases, W-bearing goethite and hematite, which were fit with the respective structures (Gualtieri and Venturelli, 1999; Blake et al., 1966), in which one Fe was replaced by W. The exact W-O and W-Fe distances obtained from the fit for the different models, including Δr and σ^2 for all paths, are given in Table 3.1 (goethite) and 3.2 (hematite).

For the goethites' first and second W-O path, the absorber atom (W) is surrounded by six oxygen atoms with W-O distance between 1.774 ±0.009 and 2.10 ±0.01 Å for the natural, and 1.781 ±0.001 to 2.12 ±0.01 Å (all corrected for phase shift) for the synthetic samples. This significant distortion of the WO_6-octahedron is consistent with our observation in the near-edge region of the X-ray absorption spectrum and was reported in previous investigations (Cid-Dresdner and Escobar 1968; Macavei and Schulz 1993).

Beyond the first six oxygen atoms, goethite shows a relatively broad and split feature at about 2.3-3.6 Å (uncorrected for phase shift) (see Fig. 5a). The splitting of this feature can be

attributed to the difference in distance between the edge (2 Fe at ~3.01 and 2 Fe at ~3.29 Å) and corner-sharing (4 Fe at 3.43 Å) Fe atoms adjacent to the absorber. Typically, for pure goethite measured at the Fe *K* edge, the first segment of the split feature at about 2.6 Å (uncorrected for phase shift) displays higher amplitude compared to the second segment at about 3.2 Å (uncorrected for phase shift) (Jiang et al. 2013).

In the case of our W-bearing goethite, however, this proportion is inverse. The first segment possesses significantly less amplitude compared to the second (see Fig. 5a). This decrease in amplitude, best visible for sample SYN-goe$_{0.05\text{-}1.6;70°C}$ and GR$_{G\text{-}I}$, suggests the formation of Fe vacancies close to the absorber and supports our chemical analyses. Accordingly, during the fitting of sample SYN-goe$_{0.05\text{-}1.6;70°C}$ and GR$_{G\text{-}I}$, the removal of one of the closest adjacent Fe atoms (typically located at 3.01 Å) improved the fit significantly, while the best fit was achieved by removing one additional Fe atom edge-sharing to W (located at 3.29 Å).

For the hematites' first and second W-O path, the absorber atom (W) is also coordinated by six O atoms with unequal W-O distances, like observed for goethite, with 1.822 ±0.004 to 2.100 ±0.008 Å for the natural, and 1.845 ±0.004 to 2.087 ±0.009 Å (both corrected for phase shift) for the synthetic samples.

In the hematite structure, $Fe^{3+}O_6^{9-}$-octahedra are either connected by face-, edge-, or corner-sharing. Since no natural or synthetic compound with face-sharing W^{6+} or Fe^{3+}-W^{6+}-octahedra is known, the closest face-sharing Fe^{3+}-atom, next to the W^{6+}-octahedron, was removed from the model, which significantly improved the fit. According to our chemical data, W replaces about 3 Fe atoms. During the fitting, we therefore included and excluded one additional Fe atom adjacent to W, typically located in a distance of about 2.97 Å from the substituted Fe^{3+} (Blake et al. 1966). Similarly to goethite, the best fit could be achieved by removing two Fe atoms adjacent to W, typically located at about 2.90 and 2.97 Å (Blake et al. 1966). However, the removed Fe atom at

2.97 Å belongs to a group of 3 Fe which all share the same distance to W. The loss of amplitude by removing one of these 3 Fe atoms can therefore easily be compensated by decreasing the value for σ^2. In conclusion, the formation of one Fe vacancy close to W is strongly supported by the results of the EXAFS fitting, but the formation of a second Fe vacancy in hematite cannot be confirmed or ruled out with absolute certainty.

Raman spectroscopy

Raman spectroscopy was performed for the synthetic goethite samples to obtain information about possible changes in the Fe-O and O-H vibrations and to infer the W exchange mechanism, as deprotonation or Fe-vacancy formation within goethite. Raman spectra of all synthetic goethite samples are given in Fig. 6a-e.

All spectra show characteristic bands of goethite published by Cornell and Schwertmann (2003); only one single Raman-active band at ~417 cm^{-1} occurs which has not already been published for goethite (see Fig. 6d)

The Raman spectrum of the W-free sample (SYN-$goe_{0.0;70°C}$) consists of a series of narrow, well-resolved peaks at wavelengths of 247, 300, 482, 551, 640 (weak), 683, 1000, 1110 cm^{-1} and several very broad bands centered at about 1275 and 1454 cm^{-1} (Fig. 6a). In the range 330-450 cm^{-1} are well-resolved peaks at 387 (strongest peak), 401 (shoulder) and 417 cm^{-1} (Fig. 6d).

With increasing tungsten content, all peaks become broader, the major peak at 387 slightly shifts to 392 cm^{-1} and the intensities and asymmetries of the bands in the range 580-780 cm^{-1} and in the very broad band at 1200-1400 cm^{-1} slightly increase (Fig. 6a; fits in Fig. 6b-e). In Fig. 6b three bands can be distinguished for the 1200-1400 cm^{-1} region at 1350, 1310 and 1255 cm^{-1} of the SYN-$goe_{0.0;70°C}$ spectrum. Besides the nonsystematic bands at 1350 and 1255 cm^{-1} the third one's intensity relatively rises and shifts to slightly higher wavenumbers. Besides the 689 cm^{-1} band of W-free goethite in Fig. 6c, additional bands at 612 and 657 cm^{-1} occur and increase with

increasing W. Raman spectra of natural W-enriched goethites (GR_{G-I} and GR_{G-II}; Fig. A6) agree well with the spectrum of the artificial sample SYN-$goe_{1.6;70°C}$ with the highest W content.

The spectra of synthetic hematites with different W contents show no significant differences in the positions, intensity and FWHM of the peaks (Fig. A7). These spectra nicely resemble the spectrum of natural hematite GR_{H-1}, besides a shoulder at ~700 cm^{-1} seen in the spectrum of the natural material (Fig. A6). However, band fits of the 550-750 cm^{-1} region in Fig. A7 show this ~700 cm^{-1} band and also show that the 660 cm^{-1} band intensity rises relatively to the 612 cm^{-1} band at higher W concentrations.

Discussion

Chemistry of W-bearing hematite and goethite

W-bearing hematites and goethites show different chemical compositions according to their geo-environmental appearance. Samples from an environment without W mineralization show higher W concentrations in hematite than in goethite, even if they formed paragenetically (see samples BF-26; Fig. 2b and Table 2). Also, in the presence of minor W-mineralization (see sample BF-11; Fig. 2b and Table 2), W is preferably associated with hematite rather than goethite. On the contrary, synthetic iron oxides and GR samples formed in the constant presence of high W. They display an opposite trend, where goethite incorporates significantly more W (up to 5.5 mol%) than hematite.

Both the natural and synthetic formation of hematite and goethite can be linked to the precursor phase ferrihydrite (Cudennec and Lecerf 2006). If both natural sample types formed around neutral pH, the adsorption of W to ferrihydrite can be assumed to be of similar magnitude (Gustafsson 2003). Hence, the opposing behavior in W-poor (BF samples) and W-rich (GR and SYN samples) environments cannot be explained by the initial adsorption of W to the precursor phase ferrihydrite. A possible explanation is the difference in the transformation processes of ferrihydrite to hematite or goethite. According to Cudennec and Lecerf (2006) hematite forms from ferrihydrite by a topotactic solidified transformation simply accompanied by dehydration in the gel during the ageing process, whereas goethite forms via a dissolution and reprecipitation process.

Goethite, forming in an open system for W, could not retain all earlier adsorbed or absorbed W and hence, tungsten could get lost during the dissolution of ferrihydrite and reprecipitation of goethite. Analogous to octahedrally coordinated Fe of the hematite structure, ferrihydrite has already adsorbed hydrated inner sphere surface W-complexes in distorted

octahedral coordination prior to its transformation to W-hematite (Gustafsson 2003; Kashiwabara et al. 2013). The formation of W-goethite directly from the fluid is more complex because W predominantly occurs as tetrahedral coordinated WO_4^{2-} and its coordination number has to be increased first (Takeno 2005). This requires a two times protonation of this species (Cruywagen 2000).

If the system is closed for W or a rapid, high and constant supply of W exists, goethite crystallites are able to incorporate high amounts of W. Hence, if the concentration of W in the transformation fluid is high enough, goethite could incorporate the high W concentrations in situ, whereas hematite would only retain the previously adsorbed W amount from ferrihydrite.

The different slopes of $X_w^{hematite/goethite}$ with respect to increasing molar concentration of W within the synthesis fluids (see Fig. 2a) can be explained, since at low ratios the solution is diluted within dimensions where the Henry's law can be assumed and the phase stability is not affected (Mysen 1978). Accordingly, concentrations below ~25 mmol/L W in goethite and below ~40 mmol/L W in hematite indicate thermodynamically stable solid solutions. The flattening of the slope for goethite and the large variance for hematite at higher W concentrations indicate the deviation from an ideal solution behavior, where the scope of Henry's law is not applicable. We suggest that this disequilibrium between W supply and incorporation is an important pre-requisite for the formation of distinct W-phases.

Fluids which strongly vary in W content precipitate ferrihydrite with variable W concentrations. Over time, these newly formed ferrihydrite crusts, which adsorbed or incorporated W from their formation solution, will transform to hematite with distinct domains, enriched or depleted in W. In contrast, during goethite formation, W previously associated with this ferrihydrite, can be homogeneously redistributed during the dissolution-reprecipitation process and the new goethite develops a homogeneous W distribution.

It can also be speculated, that the formation pathway has a direct control on the maximum W content in hematite and goethite. In our experiments, hematite reached a limit of ~1.2 $X_W^{hematite}$ in the synthetic samples, even at concentrations of 50 mmol/L W and higher (Fig. 2a). W concentrations in hematite are therefore limited by the W previously associated with ferrihydrite, even if a later W-enriched solution would arrive. W concentration in goethite, on the other hand, is, to a certain extent, correlated to the concentration of W in solution. Obviously, due to the formation of Fe-vacancies, the W content in goethite is limited by the stability of the goethite structure to the increasing number of vacancies.

Based on the phenomena discussed above, the secondary oxi/hydroxides hematite and goethite can track the fluid history of W in W-poor geo-environments. If the synthetic experiments (Fig. 2a) are applied to the mean W contents of the Schwarzwald samples (BF, Fig. 2b), the hematite sample BF-26 formed in the presence of solutions with 21 mmol/L W, sample BF-11 at 7 mmol/L W, and the goethites BF-26 at 0.1 mmol/L W, BF-20 at 0.4 mmol/L W. For the sample BF-26 this would indicate that this goethite formed at significantly lower W concentrations than the hematite. If the results of the synthetic iron oxides (Fig. 2a) are applied to the mean W contents of the samples from Grantcharitza (GR, Fig. 2b), they would correspond to W concentrations within fluids of ~200 mmol/L W for goethite $GR_{G\text{-}I}$, 8 mmol/L W for goethite $GR_{G\text{-}II}$ and >200 mmol/L W for hematite $GR_{H\text{-}I}$. This implies that goethite $GR_{G\text{-}I}$ and hematite $GR_{H\text{-}I}$ originate from fluids with similar W concentrations. Goethite $GR_{G\text{-}II}$, however, crystallized at significantly lower concentrations, although showing the same mean W content as hematite. The presence of two different fluids is also supported by microscopic observations of the phases (cf. Appendix B1).

Because of the large variability of W in hematites grown from synthesis solutions with >20 mmol/L W, the interpretation of fluid history should be reliable for hematites containing less than

0.3-0.4 mol% W (i.e. grown in fluids <20 mmol/L W). The interpretation for goethites should be possible for much higher W concentrations, such as the ones reached by our synthesis experiments, but their use is restricted because of potential W redistribution during the ferrihydrite-goethite transformation.

The synthesis experiments showed that naturally occurring hematites and goethites from the Schwarzwald and the goethites from Bulgaria could easily have incorporated their highest W-concentrations due to former precipitation of ferrihydrite. The hematites from Bulgaria, however, exceed the maximum possible W incorporation revealed by our synthesis experiments, an observation, for which we lack an explanation.

Crystallographic parameters of W-doped hematite and goethite

The increase of W in goethite causes an increase of the cell parameter c (cf. Table 1 and Fig. A2) which happens, if the structural disorder becomes higher (Cornell and Schwertmann 2003). Increasing structural disorder is also shown by our µRS data (Fig. 6). This result is unequivocal evidence that the tungsten atoms are incorporated into the structure of goethite.

For hematite, there are no obvious correlations between cell parameters and W content (Table 1), either, because of low concentrations or because of the similarity of the ionic radii of Fe^{3+} and W^{6+} (Shannon 1976). Also Kolitsch (1998) showed that an incorporation of relatively large amounts of W is possible while no significant changes of the unit-cell parameters are caused.

XANES W L_1 and W L_3 spectra

The nature of the W octahedra can be inferred from the pre-edge intensity from the W L_1 edge spectra and the splitting of the whiteline in the W L_3 edge spectra, shown by Yamazoe et al. (2008). For a detailed description of the phenomena causing different splits and pre-edge shapes

in Fig. A8 see Appendix B6. In Fig. A8 the positions of hübnerite (C), wolframite (D), the synthetic goethite SYN-goe$_{0.05;70°C}$ and natural sample hematite BF-26 are characterized by a distorted octahedral structure because they are located about halfway between regular octahedral (lower right corner; compounds f and g) and tetrahedral coordination (upper left corner; compounds a and b) (cf. Yamazoe et al. 2008).

The W L_1 pre-edge area and the W L_3 whiteline split values of natural hematite BF-26 and goethite SYN-goe$_{0.05;70°C}$ are located close to each other. Hence, the distortion of their octahedra should be similar. The natural goethite sample BF-20 is expected to possess a somewhat higher octahedral distortion due to a ~0.5 eV smaller W L_3 whiteline split. For a detailed explanation and temperature effects accounting the distortion of the WO_6 octahedra, see Appendix B6.

XANES Fe K spectra

Self absorption-corrected Fe K XANES spectra are almost identical to a pure goethite reference spectrum for sample BF-20 and to a pure hematite reference spectrum for sample BF-11 (Fig. A5.1 and A5.2). A Fe K XANES spectrum of wolframite where all Fe is Fe^{2+} is also shown in Fig. A5.1 and A5.2 to demonstrate the edge shift for a bare Fe^{2+} reference. If per W^{6+} three Fe^{3+} are reduced to three Fe^{2+}, such a fraction is potentially too small to cause a recognizable edge shift in the Fe K-edge towards lower energy. Thus, an appreciable edge shift is linked to very high W concentrations as it is in goethite samples SYN-goe$_{1.6;70°C}$ and GR_{G-I}.

Raman spectroscopy

According to group theory analysis, goethite has 24 Raman active modes (Rousseau et al. 1981). 18 modes of vibration of O and Fe (FeO_6 octahedron modes) fall into the spectral range below 700 cm^{-1}. The remaining 6 modes (for H) are attributed to different vibrations of OH-groups. In analogy with the isostructural diaspore (AlOOH), at least 8 modes of OH bending

vibrations can be expected in the range 1000-1300 cm^{-1} (Demichelis et al. 2007). Hence, we interpret the 6 bands from ~1000 cm^{-1} to ~1350 cm^{-1} in Fig. 6b as the corresponding OH bending vibrations of goethite.

The presence of tungsten in the structure of goethite increases the structural disorder in goethite visible in the Raman spectra as broadening/displacement of the all peaks below 700 cm^{-1} (Fig. 6a,c and d) as well as in the formation of poorly resolved bands at ~880 cm^{-1} (Fig. 6a; marked by arrows) and in the 150-275 cm^{-1} region (Fig. 6e). An increasing content of tungsten in Fig. 6a does not indicate a decrease of the intensity of Raman bands in the interval 1100-1400 cm^{-1}. Moreover, the relative intensity of this spectral interval, especially for the ~1310 cm^{-1} band, is relatively higher when the tungsten content is larger (Fig. 6b). This means that a protonation mechanism for the structural incorporation of W into goethite by H^+ seems to be more probable than deprotonation.

The situation with hematite is rather different. The presence of tungsten in the hematite structure is not well visible in the Raman spectra due to the masking effect of other factors. High concentrations of vacancies in the positions of Fe atoms is an inherent feature of hematite formed under natural and laboratory conditions during topotactical transformation of ferrihydrite to hematite. In the Raman spectrum of hematite, the defect structure of the Fe-sublattice is manifested by an additional peak at about 660 cm^{-1}, besides the others allowed by group theory analysis (Bersani et al. 1999). A similar effect on Raman spectra is expected by the structural incorporation of tungsten that increases the number of vacancies in the position of Fe. According to Fig. A7 this is observed at increased W incorporation, but a clear correlation with increasing W concentrations is at first glance missing. However, Chernyshova et el. (2007) showed a particle size effect. If samples with identical particle sizes are compared (SYN-hem$_{0.00}$ to SYN-hem$_{0.4}$; both 22 nm; and SYN-hem$_{0.05}$ to SYN-hem$_{0.8}$; both 29 nm; Table 1) a positive correlation

between the W concentration and the 660 cm^{-1} band intensity emerges. Obviously, the incorporation of W into hematite enhances the Fe-sublattice distortion by the production of vacancies.

Mechanisms for the structural incorporation of W^{6+} in goethite and hematite

Goethite is built by double-chains of FeO_6-ocahedra connected by edge-sharing running parallel to *b*. Four double-chains, connected by corner sharing, form a pseudo-tunnel structure filled with hydrogen atoms for charge balance. The substitution of Fe^{3+} by W^{6+} creates three positive excess charges, which have to be compensated.

Obviously, the release of three hydrogen atoms could compensate the excess charge. At the highest W concentration in goethite $GR_{G\text{-}I}$, however, the hydrogen content would then be reduced significantly. Analogous to the structural incorporation of Sb^{5+}, this deprotonation mechanism only works for low concentrations of highly charged cations (Bolanz et al. 2013b). If the Sb concentration rises, the goethite structure would probably collapse due to missing hydrogen bonds. In analogy, temperature-induced dehydroxylation experiments show a breakdown of the goethite structure long before the depletion of the hydroxyl groups (Gualtieri and Venturelli 1999).

Based on our chemical and spectroscopic analyses, the formation of Fe^{3+} vacancies seems to be the most likely balance reaction. This would also reduce the number of edge-sharing Fe-octahedra with highly charged W^{6+}. In all natural and synthetic ferric tungstate structures (Escobar et al. 1971; Sensgas and Galy 1974; Pinto et al. 1977; Yang et al. 2003), a maximum of two octahedra are edge-sharing with the W-octahedron, and only for Fe_2WO_6 (Sensgas and Galy 1974; Pinto et al. 1977), these edge-sharing octahedra are Fe^{3+}. In the goethite structure, however, all Fe-octahedra have four edge-sharing Fe partners forming the octahedral double chains. In analogy to the above-mentioned natural and synthetic ferric tungstate structures, we assume, that

for the goethite structure the number of four hypothetic edge-sharing Fe partners adjacent to W has to be reduced to a maximum of two. This results in two vacant Fe sites in goethite adjacent to W^{6+}. Accordingly, one W would replace three Fe atoms, exactly as suggested by our chemical analyses. Obviously, this substitution produces three excess negative charges, which would have to be balanced by the protonation of the adjacent oxygen atoms, previously connected to Fe^{3+}, or by the formation of oxygen vacancies. For goethite, μRS demonstrates that the protonation seems to be the actual valence balancing process (see Eq. 4).

Eq. 4: $$3Fe^{3+} \xrightarrow{protonation\&vacancies} W^{6+} + 3H \quad + 2[\ ]^{0}$$

The hematite structure does not possess structurally bound H which could compensate for the excess charge.

Due to the isotructural relationship between hematite (Fe_2O_3) and ilmenite ($Fe^{2+}Ti^{4+}O_3$), a reduction of surrounding Fe^{3+} to Fe^{2+} was suggested for the structural incorporation of Ti^{4+} (Morin 1951; Balko and Clarkson 2001) and Ge^{4+} (Sieber et al. 1985; Bernstein and Waychunas 1987), but no Fe^{2+} could be detected by XANES.

Furthermore, as for W-bearing goethite, our chemical analyses suggest, that for each W nearly three Fe atoms leave the structure. In addition to the specific atomic position where W substitutes Fe, also the next closest Fe atom with a distance of 2.9 Å is highly unlikely to stay in the hematite structure. To our knowledge, no natural or synthetic structure displays face-sharing Fe^{3+}-W^{6+} or even W^{6+}- W^{6+} octahedra. Additionally, as in goethite, the number of edge-sharing Fe-octahedra would have to be reduced by one. This results in a total loss of three Fe atoms for one W^{6+}. As in the case of goethite, either the protonation of O^{2-} atoms by H^{+} or the formation of O^{2-}-vacancies could compensate for the excess negative charge. As already obtained for hematite grown from precursor ferrihydrite, protonated oxygen and Fe^{3+}-vacancies are more likely (Wolska 1981, 1988; Wolska and Szajda 1985).

726

Implications

The combination of chemical and spectroscopic techniques as well as the consideration of the different processes involved during maturation of ferrihydrite to hematite or goethite imply that oscillatory-zoned, W-bearing hematite records the chemical evolution of a fluid and allows to distinguish different fluid batches. Botryoidal hematite formed as solid transformation from the precursor phase ferrihydrite can record the fluid history of a W-bearing fluid (both in W-enriched and W-poor environments), as hematite inherits the W content of the precursor ferrihydrite. Thus, hematite is able to record differences in W content in a fluid and retain this information over geologically long periods of time. In contrast, goethite only records the W concentrations, which prevailed at the time of its crystallization, i.e., during goethite formation from ferrihydrite. In combination: hematite records the W concentrations in a fluid during ferihydrite precipitation, goethite during ferrihydrite maturation.

The W fraction incorporated into goethite depends on the W concentration in the system. This involves mixing processes of W from dissolving ferrihydrite, W present in the actual fluid and a complex relationship between the adsorption potential of goethite, its crystal size/morphology and its precipitation rate. These interactions cannot be evaluated yet. For hematite containing less than 0.4 mol% W, the adsorption potential of W to ferrihydrite appears to be the most important parameter for W incorporation.

Our investigations indicate that the incorporation of W into hematite and goethite takes place as a heterovalent substitution of one W for three Fe atoms into their crystal structure. Hence, W is, once incorporated, immobilized for as long as these phases are stable. Lastly, it should be noted that W-bearing iron-oxi(hydroxi)des, formed in the oxidation zones of W deposits, represent potentially economic W resources.

Acknowledgements

We are grateful to Thomas Wenzel (Tübingen) for his professional assistance during EMPA analysis, Michael Marks (Tübingen) for his help during the TXRF analysis, Melanie Keuper (Tübingen) for her instructions during µRS measurements, Christoph Berthold and Nadja Wichtner for performing µXRD measurements, Udo Neumann (Tübingen) for his friendly assistance during ore microscopy, Indra Gill-Kopp (Tübingen) for the professional preparation of the thin sections, and finally Maximilian Keim and Benjamin Walter (Tübingen) for numerous discussions and help during sampling. We would also like to thank Juraj Majzlan (Jena) in whose laboratories pXRD and EMPA measurements were perfomed. We thank the Karlsruher Institute for Technelogy and spcifically the Angströmquelle Karlsruhe (ANKA) for the granted beamtime.

References

Alvarez, M., Sileo, E.E., and Rueda, E.H. (2008) Structure and reactivity of synthetic Co-substituted goethites. American Mineralogist, 93, 584-590.

Baatartsogt, B., Schwinn, G., Wagner, T., Taubald, H., Beitter, T., and Markl, G. (2007) Contrasting paleofluid systems in the continental basement: a fluid inclusion and stable isotope study of hydrothermal vein mineralization, Schwarzwald district, Germany. Geofluids, 7, 123-147.

Balko, B.A., and Clarkson, K.M. (2001) The effect of doping with Ti(IV) and Sn(IV) on oxygen reduction at hematite electrodes. Journal of the Electrochemical Society, 148, E85-E91.

Benvenuti, M., Dini, A., D'Orazio, M., Chiarantini, L., Corretti, A., and Costagliola, P. (2013) The tungsten and tin signature of iron ores from Elba island (Italy): A tool for provenance studies of iron production in the Mediterranean region. Archaeometry, 55, 479-506.

Bernstein, L.R., and Waychunas, G.A. (1987) Germanium crystal chemistry in hematite and goethite from the Apex Mine, Utah, and some new data on germanium in aqueous solution and in stottite. Geochimica et Cosmochimica Acta, 51, 623-630.

Bersani, D., Lottici, P.P., and Montenero, A. (1999) Micro-Raman investigation of iron oxide films and powders produced by sol–gel syntheses. Journal of Raman spectroscopy, 30, 355-360.

Blake, R.L., Hessevick, R.E., Zoltai, T, and Fingter, L.W. (1966) Refinement of the hematite structure. American Mineralogist, 51, 123-129.

Bolanz, R.M., Wierzbicka-Wieczorek, M., C□aplovic□ová, M., Uhlík, P., Go□ttlicher, J., Steininger, R., and Majzlan, J. (2013a) Structural incorporation of As^{5+} into hematite. Environmental science and technology, 47, 9140-9147.

Bolanz, R.M., Bläss, U., Ackermann, S., Ciobotă, V., Rösch, P., Tarcea, N., Popp, J., and Majzlan, J. (2013b) The effect of antimonate, arsenate, and phosphate on the transformation of

ferrihydrite to goethite, hematite, feroxyhyte, and tripuhyite. Clays and Clay Minerals, 61, 11-25.

Brinza, L., Vu, H.P., Shaw, S., Mosselmans, J.F.W., and Benning, L.G. (2015) Effect of Mo and V on the Hydrothermal Crystallization of Hematite from Ferrihydrite: An in Situ Energy Dispersive X-ray Diffraction and X-ray Absorption Spectroscopy Study. Crystal Growth & Design, 15, 4768-4780.

Cantaluppi, C., Natali, M., Ceccotto, F., and Fasson, A. (2013) Multielemental analysis of powder samples by direct measurement with TXRF. X-Ray Spectrometry, 42, 213-219.

Chernyshova, I.V., Hochella, M.F. Jr., and Madden, A.S. (2007) Size-dependent structural transformations of hematite nanoparticles. 1. Phase transition. Physical Chemistry Chemical Physics, 9, 1736-1750.

Ciobanu, C.L., Cook, N.J., Kelson, C.R., Guerin, R., Kalleske, N., and Danyushevsky, L. (2013) Trace element heterogeneity in molybdenite fingerprints stages of mineralization. Chemical Geology, 347, 175-189.

Cid-Dresdner, H., and Escobar, C. (1968) The crystal structure of ferberite, $FeWO_4$. Zeitschrift für Kristallographie-Crystalline Materials, 127, 61-72.

Cornell, R.M., and Schwertmann, U. (2003) The iron oxides: structure, properties, reactions, occurrences and uses, 2nd ed., 664 p. Wiley-VCH, Weinheim, germany.

Cruywagen, J. J. (2000). Protonation, oligomerization, and condensation reactions of vanadate (V), molybdate (VI), and tungstate (VI). Advances in inorganic chemistry, 49, 127-182.

Cudennec, Y., and Lecerf, A. (2006) The transformation of ferrihydrite into goethite or hematite, revisited. Journal of Solid State Chemistry, 179, 716-722.

De Faria, D.L.A., Venâncio Silva, S., and De Oliveira, M.T. (1997) Raman microspectroscopy of some iron oxides and oxyhydroxides. Journal of Raman spectroscopy, 28, 873-878.

De La Calle, I., Cabaleiro, N., Romero, V., Lavilla, I., and Bendicho, C. (2013) Sample pretreatment strategies for total reflection X-ray fluorescence analysis: A tutorial review. Spectrochimica Acta Part B: Atomic Spectroscopy, 90, 23-54.

De Leon, J.M., Rehr, J.J., Zabinsky, S.I., and Albers, R. (1991) Ab initio curved-wave x-ray-absorption fine structure. Physical Review B, 44, 4146.

Demichelis, R., Noel, Y., Civalleri, B., Roetti, C., Ferrero, M., Dovesi, R. (2007) The Vibrational Spectrum of α-AlOOH Diaspore: An Ab Initio Study with the CRYSTAL Code. The Journal of Physical Chemistry B, 111, 9337-9346.

Dimitrov, S. (1981) Mineralogy of Grantcharitza tungsten deposit. – Ore-forming processes and mineral deposits, Sofia, 14-15, 35-49, (in Bulgarian)

Duff, M.C., Coughlin, J.U., and Hunter, D.B. (2002) Uranium co-precipitation with iron oxide minerals. Geochimica et Cosmochimica Acta, 66, 3533-3547.

EU Commission (2010) Critical raw materials for the EU. Report of the Ad-hoc Working Group on defining critical raw materials (Online). Available: http://ec.europa.eu/growth/sectors/raw-materials/specific-interest/critical/index_en.htm (accessed January 7, 2016). European Commission

Escobar, C., Cid-Dresdner, H., Kittl, P. and Dumler, I. (1971) The relation between 'light wolframite' and common wolframite. American Mineralogist, 56, 489-498

Faisi, S., 1951. Die Eisen-und Manganerzgänge von Eisenbach (südöstlicher Schwarzwald) und ihre tektonische Stellung. Neues Jahrbuch für Mineralogie – Abhandlungen: Journal of Mineralogy and Geochemistry, 83, p. 53-150 (in German).

Gehlen, K. von (1958) U- und W-haltiger Hollandit und Kryptomelan von Eisenbach (südöstl. Schwarzwald). Neues Jahrbuch für Mineralogie: Monatshefte, 4, p. 73-84 (in German).

Gualtieri, A.F., and Venturelli, P. (1999) In situ study of the goethite-hematite phase transformation by real time synchrotron powder diffraction. American Mineralogist, 84, 895-904.

Gustafsson, J.P. (2003) Modelling molybdate and tungstate adsorption to ferrihydrite. Chemical Geology, 200, 105-115.

Haase, C.S., Chadam, J., Feinn, D., and Ortoleva, P. (1980) Oscillatory zoning in plagioclase feldspar. Science, 209, 272-274.

Hsin, K., Sheng, Y., Harding, M.M., Taylor, P.A., and Walkinshaw, M.D. (2008) MESPEUS: a database of the geometry of metal sites in proteins. Journal of Applied Crystallography, 41, 963-968.

Jambor, J.L., and Dutrizac, J.E. (1998) Occurrence and constitution of natural and synthetic ferrihydrite, a widespread iron oxyhydroxide. Chemical Reviews, 98, 2549-2586.

Jamtveit, B. (1991) Oscillatory zonation patterns in hydrothermal grossular-andradite garnet; nonlinear dynamics in regions of immiscibility. American Mineralogist, 76, 1319-1327.

Jamtveit, B., and Hervig, R.L. (1994) Mass transport and chemical reaction kinetics in hydrothermal systems recorded by intracrystalline mineral zonation. Science, 263, 505-508.

Jamtveit, B., Wogelius, R.A., and Fraser, D.G. (1993) Zonation patterns of skarn garnets: Records of hydrothermal system evolution. Geology, 21, 113-116.

Jamtveit, B., Agnarsdottir, K.V., and Wood, B.J. (1995). On the origin of zoned grossular-andradite garnets in hydrothermal systems. European Journal of Mineralogy, 1399-1410.

Jiang, S., Kim, M.G., Kim, I.Y., Hwang, S.J., and Hur, H.G. (2013) Biological synthesis of free-standing uniformed goethite nanowires by Shewanella sp. HN-41. Journal of Materials Chemistry A, 1, 1646-1650.

Kamenov, B., Peytcheva, I., Klain, L., Arsova, K., Kostitsin, Y, and Salnikova, E. (1999) Rila-West Rhodopes Batholith: Petrological and geochemical constraints for its composite character. - Geochemistry, Mineralogy and Petrology, Sofia, 36, 3-27.

Kashiwabara, T., Takahashi, Y., Marcus, M. A., Uruga, T., Tanida, H., Terada, Y., and Usui, A. (2013). Tungsten species in natural ferromanganese oxides related to its different behavior from molybdenum in oxic ocean. Geochimica et Cosmochimica Acta, 106, 364-378.

Kirchheimer, F. (1953) Weitere Untersuchungen über das Vorkommen von Uran im Schwarzwald. Abhandlungen des Geologischen Landesamtes Baden-Württemberg, 1, p. 1-60 (in German).

Klementiev, K.V. (2012) XAFSmass. A program for calculating the mass of XAFS samples (Online). Available: https://intranet.cells.es/Beamlines/CLAESS/software/xafsmass.html (accessed January 7, 2016). CELLS – ALBA, Barcelona, Spain.

Kolitsch, U. (1998) Bernalite from the Clara mine, Germany, and the incorporation of tungsten in minerals containing ferric iron. Canadian Mineralogist, 36, 1211-1216.

Koutsospyros, A., Braida, W., Christodoulatos, C., Dermatas, D., and Strigul, N. (2006) A review of tungsten: from environmental obscurity to scrutiny. Journal of Hazardous Materials, 136, 1-19.

Kuzmin, A., and Purans, J. (1993) The influence of the focusing effect on the x-ray absorption fine structure above all the tungsten L edges in non-stoichiometric tungsten oxides. Journal of Physics: Condensed Matter, 5, 9423-9430.

Lüders, V. (1994) Geochemische Untersuchungen an Gangartmineralen aus dem Bergbaurevier Freiamt-Sexau und dem Badenweiler Quarzriff (Schwarzwald). Abhandlungen des Geologischen Landesamtes Baden-Württemberg, 14, p. 173-190. Geologisches Landesamt Baden-Württemberg, Freiburg i.B., Germany (in German).

Macavei, J., and Schulz, H. (1993) The crystal structure of wolframite type tungstates at high pressure. Zeitschrift für Kristallographie-Crystalline Materials, 207, 193-208.

Manning, C.E., and Bird, D.K. (1990) Fluorian garnets from the host rocks of the Skaergaard intrusion: Implications for metamorphic fluid composition. American Mineralogist, 75, 859-873.

Markl, G., Blanckenburg, F. von, and Wagner, T. (2006) Iron isotope fractionation during hydrothermal ore deposition and alteration. Geochimica et Cosmochimica Acta, 70, 3011-3030.

Marshall, T.A., Morris, K., Law, G.T., Livens, F.R., Mosselmans, J.F.W., Bots, P., and Shaw, S. (2014) Incorporation of uranium into hematite during crystallization from ferrihydrite. Environmental Science & Technology, 48, 3724-3731.

Metz, R. (1977) Mineralogisch-landeskundliche Wanderungen im Nordschwarzwald: besonders in dessen alten Bergbaurevieren. Der Aufschluss Sonderheft, 20, 516 p. Schauenburg Verlag, Lahr, Germany (in German).

Metz, R., Richter, M., and Schürenberg, H. (1957) Die Blei-Zink-Erzgänge des Schwarzwaldes. Beihefte zum Geologischen Jahrbuch, 29. 277 p. Schweizerbart science publishers, Stuttgart, Germany (in German).

Michel, F.M., Ehm, L., Antao, S.M., Lee, P.L., Chupas, P.J., Liu, G., and Parise, J.B. (2007) The structure of ferrihydrite, a nanocrystalline material. Science, 316, 1726-1729.

Mitsunobu, S., Takahashi, Y., Terada, Y., and Sakata, M. (2010) Antimony (V) incorporation into synthetic ferrihydrite, goethite, and natural iron oxyhydroxides. Environmental Science & Technology, 44, 3712-3718.

Morin, F.J. (1951) Electrical Properties of α-Fe_2O_3 and α-Fe_2O_3 Containing Titanium. Physical Review, 83, 1005.

Mysen, B.O. (1978) Limits of solution of trace elements in minerals according to Henry's Law: Review of experimental data. Geochimica et Cosmochimica Acta, 42, 871-885.

Nico, P.S., Stewart, B.D., and Fendorf, S. (2009) Incorporation of oxidized uranium into Fe (hydr) oxides during Fe (II) catalyzed remineralization. Environmental Science & Technology, 43, 7391-7396.

Pfaff, K., Romer, R.L., and Markl, G. (2009) U-Pb ages of ferberite, chalcedony, agate, 'U-mica' and pitchblende: constraints on the mineralization history of the Schwarzwald ore district. European Journal of Mineralogy, 21, 817-836.

Pinto, H., Melamud, M., and Shaked, H. (1977) Magnetic structure of Fe_2WO_6, a neutron diffraction study. Acta Crystallographica A, 33, 663-667.

Putnis, A., Fernandez-Diaz, L., and Prieto, M. (1992) Experimentally produced oscillatory zoning in the $(Ba,Sr)SO_4$ solid solution. Nature, 358, 743-745.

Ravel, Á., and Newville, M. (2005) ATHENA, ARTEMIS, HEPHAESTUS: data analysis for X-ray absorption spectroscopy using IFEFFIT. Journal of Synchrotron Radiation, 12, 537-541.

Rousseau, D.L., Bauman, R.P., and Porto, S.P.S. (1981) Normal mode determination in crystals. Journal of Raman Spectroscopy, 10, 253-290.

Schatz, R.H. (1970) Scheelitführende Eisenerze der Grube Rappenloch bei Eisenbach im mittleren Schwarzwald. Der Aufschluss, 21, p. 294-298. Vereinigung der Freunde der Mineralogie und Geologie, Göttingen, Germany (in German).

Scheinost, A.C., Rossberg, A., Vantelon, D., Xifra, I., Kretzschmar, R., Leuz, A.K., and Johnson, C.A. (2006) Quantitative antimony speciation in shooting-range soils by EXAFS spectroscopy. Geochimica et Cosmochimica Acta, 70, 3299-3312.

Shannon, R.T. (1976) Revised effective ionic radii and systematic studies of interatomic distances in halides and chalcogenides. Acta Crystallographica Section A, 32, 751-767.

Schwertmann, U. (1964) Differenzierung der Eisenoxide des Bodens durch Extraktion mit Ammoniumoxalat-Lösung. Zeitschrift für Pflanzenernährung, Düngung, Bodenkunde, 105, 194-202 (in German).

Schwertmann, U., and Cornell, R.M. (2000) Iron Oxides in the Laboratory: Preparation and Characterization, 2nd ed., 204 p. Wiley-VCH, Weinheim, Germany.

Sensgas, J., and Galy, J. (1974) L'oxyde double Fe_2WO_6. I. Structure cristalline et filiation structural. Journal of Solid State Chemistry, 10, 5-11 (in French).

Sieber, K.D., Sanchez, C., Turner, J.E., and Somorjai, G.A. (1985) Preparation, electrical and photoelectrochemical properties of magnesium doped iron oxide sintered discs. Materials Research Bulletin, 20, 153-162.

Smith, R.M., Martell, A.E., and Motekaitis, R.J. (2001) NIST Critically Selected Stability Constants of Metal Complexes Database. Version 6.0. NIST Standard Reference Database, vol. 46. National Institute of Standards and Technology, US Department of Commerce, Gaithersburg.

Stosnach, H. (2010) Analytical determination of selenium in medical samples, staple food and dietary supplements by means of total reflection X-ray fluorescence spectroscopy. Spectrochimica Acta Part B: Atomic Spectroscopy, 65, 859–863.

Szymański, J.T., and Roberts, A.C. (1984) The Crystal Structure of Tungstite, $WO_3{\cdot}H_2O$. Canadian Mineralogist, 22, 681-688.

Takeno, N. (2005). Atlas of Eh-pH diagrams - Intercomparison of thermodynamic databases. Geological survey of Japan open file report, 419, 272-273.

Tarassov, M., Mihailova, B., Tarassova, E., and Konstantinov, L. (2002) Chemical composition and vibrational spectra of tungsten-bearing goethite and hematite from Western Rhodopes, Bulgaria. European Journal of Mineralogy, 14, 977-986.

Walenta, K. (1963) Wolframmineralien aus dem Schwarzwald. Jahreshefte des Geologischen Landesamtes Baden-Württemberg, 6, p. 105-112. Geologisches Landesamt Baden-Württemberg, Freiburg i.B., Germany (in German).

Werner, W., and Franzke, H. (1994) Tektonik und Mineralisation der Hydrothermalgänge am Schwarzwaldrand im Bergbaurevier Freiamt-Sexau. Abhandlungen des Geologischen Landesamtes Baden-Württemberg, 14, p. 27-98. Geologisches Landesamt Baden-Württemberg, Freiburg i.B., Germany (in German).

Werner, W., Schlaegel-Blaut, P., and Rieken, R. (1990) Verbreitung und Ausbildung von Wolfram-Mineralisationen im Kristallin des Schwarzwaldes. Jahreshefte des Geologischen Landesamtes Baden-Württemberg, 32, p. 17-61. Geologisches Landesamt Baden-Württemberg, Freiburg i.B., Germany (in German).

Wernicke, R.S., and Lippolt, H.J. (1993) Botryoidal hematite from the Schwarzwald (Germany): heterogeneous uranium distributions and their bearing on the helium dating method. Earth and Planetary Science Letters, 114, 287-300.

Wernicke, R.S., and Lippolt, H.J. (1995) Direct isotope dating of a Northern Schwarzwald qtz-ba-hem vein. Neues Jahrbuch für Mineralogie: Monatshefte, 4, p. 161-172 (in German).

Wimmenauer, W. (1955) Über den Mineralbestand uranhaltiger Manganerze von Eisenbach und einiger anderer „Psilomelane“ des Schwarzwaldes. Jahreshefte des Geologischen Landesamtes Baden-Württemberg, 1, p. 72-78. Geologisches Landesamt Baden-Württemberg, Freiburg i.B., Germany (in German).

Wojdyr, M. (2010) Fityk: a general-purpose peak fitting program. Journal of Applied Crystallography, 43, 1126-1128.

Wolska, E. (1981). The structure of hydrohematite. Crystalline Materials, 154, 69-76.

Wolska, E. (1988). Relations between the existence of hydroxyl ions in the anionic sublattice of hematite and its infrared and X-ray characteristics. Solid State Ionics, 28, 1349-1351.

Wolska, E., & Szajda, W. (1985). Structural and spectroscopic characteristics of synthetic hydrohaematite. Journal of materials science, 20, 4407-4412.

Yamazoe, S., Hitomi, Y., Shishido, T., and Tanaka, T. (2008) XAFS Study of Tungsten L_1-and L_3-Edges: Structural Analysis of WO_3 Species loaded on TiO_2 as a Catalyst for Photo-oxidation of NH_3. The Journal of Physical Chemistry C, 112, 6869-6879.

Yang, W.B., Lu, C.Z., Lin, X., Zhuang, H.H. (2003) Syntheses, structures and magnetic properties of three new extended iron-containing heteropolytungstates. Zeitschrift für Anorganische und Allgemeine Chemie, 629, 2046-2052.

Yardley, B.W.D., Rochelle, C.A., Barnicoat, A.C., and Lloyd, G.E. (1991) Oscillatory zoning in metamorphic minerals: an indicator of infiltration metasomatism. Mineralogical Magazine, 55, 357-365.

Figure captions:

Fig. 1: Heterogeneous and homogeneous W-distribution in hematite from the Schwarzwald. (a-b) Typical heterogeneous W-distribution between W-rich hem-I and hem-II, BF-11. Note relic siderite morphology with porous hematite inside (marked in blue). Bright green-red regions of secondary Y(±REE)-phosphate are misinterpret cause of W Lα and Y Kα overlap (b upper right; colored about 300-440 cps). Regions of homogeneous distributions used for XAFS measurements (c-d) hematite in BF-11, (e-f) hematite in BF-26 and (g-h) goethite in BF-20. (a) Microphotograph, reflected light, slightly dejusted polarizers, (b, d, f, h) W-distribution maps of the W Lα fluorescence, (c, e, g) BSE-images in COMPO-mode. White arrows indicate growth directions of hematite or goethite crystallites.

Fig. 2: W concentrations within hematite (red) and goethite (brown) used in this study as molar fraction χ of W in hematite and goethite, respectively. For calculation of χ see Eq. 2. a) synthetic samples are given as EMPA data (crosses) and TXRF data (squares) versus their initial molar W/Fe ratios (lower scale; 0.00, 0.05, 0.1, 0.2, 0.4, 0.8 and 1.6) and appropriate W concentrations (upper scale) within the fluids during their synthesis. Error bars in black indicate the relative error of the TXRF analysis of 10%, the crosses the variation of the single EMPA measurements. b) EMPA data of the natural samples as variation of each single measurement (crosses). In a) and b) mean values marked in black and median values in white. Samples description in the lower part: BF samples from W-free/minor W deposits, GR samples from scheelite vein. Indexes of the SYN samples express the molar W/Fe ratios during synthesis. The grey shaded areas represent the interpolated overlap of TXRF and EMPA data. Dotted lines show the trends of W incorporation by EMPA mean values, indicating different slopes of hypothetic solid solutions at highly diluted W synthesis fluids.

Fig. 3: W L_3 μ-XANES spectra of natural (a) hematite (BF-26), (b) goethite (BF-20), (c) synthetic hematite (SYN-hem$_{0.05}$), (d) and (e) synthetic goethites (solid line SYN-goe$_{0.05;70°C}$, dashed line SYN-goe$_{0.05;25°C}$, respectively). Samples are compared to XANES spectra of reference (f) $MnWO_4$ (hübnerite), (g) (Fe,Mn)WO_4 (wolframite): WO_6 octahedra; and (h) $CaWO_4$ (scheelite), and (i) $Na_2WO_4{\cdot}2H_2O$: WO_4 tetrahedra. Natural and synthetic samples were measured at thin sections and at pellets in fluorescence mode and the reference materials at pellets in transmission. The spectra of the hematite sample BF-26 with higher energy resolution is given a dotted line.

Fig. 4: W L_1 μ-XANES spectra of (a) natural hematite (BF-26) and (b) synthetic goethite (SYN-goe$_{0.05;70°C}$). Samples compared to XANES transmission spectra of reference (c) $MnWO_4$ (hübnerite), (d) (Fe,Mn)WO_4 (wolframtie), both WO_6 octahedra and (e) $CaWO_4$ (scheelite), (f) $Na_2WO_4{\cdot}2H_2O$, both WO_4 tetrahedra. Samples were mesured at thin section and pellet in fluorescence mode and the reference materials at pellets in transmission. For natural goethite and SYN-goe$_{0.05;25°C}$ and SYN-hem$_{0.5}$ fluorescence emission was weak to measure L_1 edge spectra in reasonable time. (A) indicates the pre-edge 2s(W) to 5d(W) + 2p(O) transition (2p(O)-5d(W) mixing), (B) the edge (2s(W) to 6p(W) + 2p(O) transition to the continuum), (C) and (D) multiple scattering.

Fig. 5: k^3-weighted W L_3-edge EXAFS spectra (left), real part Fourier transform W L_3-edge EXAFS spectra (middle) and magnitude of the Fourier transform (right). (a) goethites SYN-goe$_{0.05\text{-}1.6;70°C}$ (synthesized at 70°C), SYN-goe$_{0.05;25°C}$ (synthesized at 25°C), BF-20, and $GR_{G\text{-}I}$. (b) hematites SYN-hem$_{0.05\text{-}1.6}$ (synthesized at 500°C), BF-26 and BF-11. The measured data is

indicated by the dotted lines, whereas the corresponding fit is indicated by the solid lines. R-space uncorrected for phase shift.

Fig. 6: Raman spectra of the synthetic goethite samples with increasing W concentration from bottom to top: SYN-goe$_{0.00;70°C}$, SYN-goe$_{0.05;70°C}$,SYN-goe$_{0.1;70°C}$, SYN-goe$_{0.2;70°C}$, SYN-goe$_{0.4;70°C}$, SYN-goe$_{0.8;70°C}$ and SYN-goe$_{1.6;70°C}$. (a) whole spectra; (b) curve fit of the OH bending modes at 1500-900 cm^{-1} range; (c) curve fit of 780-580 cm^{-1}range; (d) curve fit of 450-330 cm^{-1} range; (e) range of 275-150 cm^{-1}. For the spectra fits, dashed lines represent the fitting peaks, red solid lines their accumulation and bold solid lines the fitted data.

Tables:

Table 1: Lattice parameters of powder samples hematite (BF-26 and SYN-hem$_{0.00\text{-}1.6}$) and goethite (SYN-goe$_{0.00\text{-}1.6}$) compared to their respective W-concentrations. Additionally the table compares Fe_2O_3 and WO_3 chemistry determined by TXRF and EMPA (cf. Fig. 2). The Fe-loss per incorporated W, calculated by Eq. 1, is shown for the TXRF results of the synthetic samples. Table 2 shows the detailed chemistry of all natural samples. [a, b]

		Lattice parameters						TXRF - Iron-loss					EMPA			
Sample	**phase**	**a** [Å]	**b** [Å]	**c** [Å]	**cryst.** [nm]	**Rwp**	**GOF**	**Fe_2O_3** [wt%]	**WO_3** [wt%]	**total** [wt%]	**N**[g]	**Fe−loss**	**Fe_2O_3** [wt%]	**WO_3** [wt%]	**total** [wt%]	**N**[g]
BF-26 I	hem	5.0357		13.7569	61	4.26	1.13	NM	bdl[c]	-	3	-	NM	NM	-	-
BF-26 II	hem	5.0366		13.7601	75	5.82	1.56	NM	0.23[c]	-	3	-	NM	NM	-	-
BF-26 III	hem	5.0362		13.7599	79	6.66	1.79	NM	0.60[c]	-	3	-	NM	NM	-	-
BF-26 IV	hem	5.0362		13.7577	77	5.92	1.57	NM	0.62[c]	-	3	-	NM	NM	-	-
BF-26 V	hem	5.0365		13.7591	76	6.00	1.59	NM	0.76[c]	-	3	-	NM	NM	-	-
BF-26 VI	hem	5.0367		13.7583	79	5.58	1.49	NM	1.19[c]	-	3	-	95.87[f]	1.05[f]	100.27	21
BF-26 VII	hem	5.0364		13.7571	82	6.00	1.57	NM	1.53[c]	-	3	-	95.47[f]	1.37[f]	99.55	20
SYN-hem$_{0.00}$	hem	5.0391		13.7613	22	6.38	1.30	99.6[d]	bdl[d]	99.6	2	-	67.88[e]	bdl[e]	68.26	10
SYN-hem$_{0.05}$	hem	5.0387		13.7575	29	6.21	1.35	97.8[d]	0.2[d]	98.0	2	2.69	66.63[e]	0.24[e]	67.19	10
SYN-hem$_{0.1}$	hem	5.0392		13.7578	25	6.43	1.38	100.4[d]	0.5[d]	100.9	2	2.81	63.84[e]	0.43[e]	64.56	10
SYN-hem$_{0.2}$	hem	5.0400		13.7605	26	6.51	1.34	99.8[d]	1.2[d]	101.0	3	2.86	76.89[e]	1.11[e]	78.39	10
SYN-hem$_{0.4}$	hem	5.0400		13.7652	22	6.37	1.27	94.4[d]	1.8[d]	96.2	3	2.88	75.51[e]	1.69[e]	77.64	10
SYN-hem$_{0.8}$	hem	5.0409		13.7637	29	6.44	1.36	97.7[d]	2.2[d]	99.9	3	2.88	79.21[e]	1.99[e]	81.55	20
SYN-hem$_{1.6}$	hem	5.0398		13.7620	38	6.50	1.36	101.2[d]	1.7[d]	103.0	3	2.87	80.45[e]	2.69[e]	83.40	10
SYN-goe$_{0.00;70°C}$	goe	9.9606	3.0240	4.6101	33	6.63	1.36	93.7[d]	bdl[d]	93.7	3	-	48.86[e]	bdl[e]	49.08	11
SYN-goe$_{0.05;25°C}$	goe	9.9653	3.0241	4.6122	31	6.98	1.47	83.5[d]	3.0[d]	86.5	3	2.90	48.30[e]	1.56[e]	50.08	28
SYN-goe$_{0.05;70°C}$	goe	NM	NM	NM	NM	NM	NM	NM	NM	NM	-	-	53.08[e]	1.86[e]	55.20	14
SYN-goe$_{0.1;70°C}$	goe	9.9644	3.0238	4.6145	47	6.36	1.38	83.6[d]	4.9[d]	88.5	3	2.90	45.46[e]	2.54[e]	48.22	10
SYN-goe$_{0.2;70°C}$	goe	9.9652	3.0238	4.6172	66	6.22	1.35	83.1[d]	5.0[d]	88.1	2	2.90	53.56[e]	3.96[e]	57.74	13
SYN-goe$_{0.4;70°C}$	goe	9.9665	3.0237	4.6210	102	5.92	1.33	78.8[d]	8.8[d]	87.6	3	2.90	60.50[e]	8.19[e]	68.94	10
SYN-goe$_{0.8;70°C}$	goe	9.9658	3.0232	4.6211	65	6.83	1.22	83.2[d]	7.7[d]	90.9	1	2.90	66.31[e]	6.65[e]	73.24	17
SYN-goe$_{1.6;70°C}$	goe	9.9630	3.0235	4.6243	45	7.08	1.21	68.8[d]	10.3[d]	79.0	2	2.90	61.47[e]	8.51[e]	70.33	21

[a] bdl = signal detected but below detection limit; [b] NM = not measured ; [c] TXRF bulk analysis of solid powder samples. Here a quantification of Fe_2O_3 is not possible due to self-absorption effects; [d] TXRF bulk analysis of solved powder samples; [e] EMPA data of resinated and polished powder samples; [f] EMPA data of polished thin sections. Deficit to total according to oxide components not presented (cf. Table 2); [g] Number of measurements.

Table 2: Representative chemical results of the natural hematite/goethite samples by EMPA characterization. The data is given as mean values in wt% of the respective element oxides. The variation of the chemistry of each sample in respect to W and the comparison between the EMPA and TXRF data is shown in Fig. 2

		EMPA [wt%]												
Sample	Phase	WO_3	Fe_2O_3	MnO	Al_2O_3	MgO	Sb_2O_5	P_2O_5	As_2O_5	MoO_3	CaO	SiO_2	total	N
BF-20	goe	0.20	79.29	0.19	0.24	0.025	0.17	0.98	0.34	bdl	0.05	4.12	85.52	53
BF-11	hem	0.45	93.79	0.15	0.37	0.017	0.19	0.02	1.17	0.10	0.10	0.86	97.17	255
BF-26	hem	1.38	92.64	0.30	0.60	0.16	0.05	0.32	0.70	bdl	0.10	0.98	97.33	229
BF-26	goe	0.04	79.71	0.62	0.09	0.037	bdl	0.42	0.06	bdl	0.03	2.92	83.88	60
$GR_{G\text{-}II}$	goe	3.65	79.40	0.01	0.29	0.023	NM	1.45	0.40	NM	0.04	1.94	86.80	18
$GR_{G\text{-}I}$	goe	11.81	74.71	0.01	0.26	0.025	NM	1.14	bdl	NM	0.07	1.32	89.33	26
$GR_{H\text{-}I}$	hem	3.84	86.53	bdl	0.26	0.018	NM	0.46	bdl	NM	0.03	2.09	93.23	8

bdl = signal detected but below detection limit; NM = element not measured; hem = hematite; goe = goethite; N = number of measurements

Table 3.1: Interatomic distances, Δr, and σ^2 of W-bearing goethite fit to sample GR_{G-I}, BF-20, SYN-$goe_{0.05-1.6;70°C}$ and SYN-$goe_{0.05;25°C}$.

GR_{G-I}				BF-20				$SYN\text{-}goe_{0.05;70°C}$				$SYN\text{-}goe_{0.05;25°C}$			
path	N	R [Å]	σ^2	path	N	R [Å]	σ^2	path	N	R [Å]	σ^2	path	N	R [Å]	σ^2
W-O	4	1.928±0.006	0,008	W-O	4	1.774±0.009	0,007	W-O	4	1.812±0.005	0,007	W-O	4	1.781±0.001	0,007
W-O	2	2.10±0.01	0,008	W-O	2	2.10±0.02	0,007	W-O	2	2.12±0.01	0,007	W-O	2	2.12±0.01	0,007
W-Fe	1	2.94±0.03	0,012	W-Fe	1	2.857±0.009	0,015	W-Fe	1	2.98±0.02	0,010	W-Fe	1	2.87±0.001	0,015
W-O	1	3.36±0.02	0,012	W-O	1	3.35±0.02	0,015	W-O	1	3.36±0.01	0,010	W-O	1	3.37±0.02	0,015
W-Fe	1	3.43±0.02	0,012	W-Fe	1	3.43±0.02	0,015	W-Fe	1	3.44±0.01	0,010	W-Fe	1	3.44±0.02	0,015
W-Fe	4	3.57±0.02	0,012	W-Fe	4	3.57±0.02	0,015	W-Fe	4	3.58±0.01	0,010	W-Fe	4	3.58±0.02	0,015
ΔE_0 = 1.7, N_{var} = 15, N_{ind} = 20.2, *R* = 0.025, *k* range = 3.6-11.6, R range = 1-4, window type: Hanning				ΔE_0 = -0.7, N_{var} = 14, N_{ind} = 18.77, *R* = 0.017, *k* range = 2.5-10, R range = 1-4, window type: Hanning				ΔE_0 = 2.5, N_{var} = 15, N_{ind} = 21.3, *R* = 0.022, *k* range = 3-11.5, R range = 1-4, window type: Hanning				ΔE_0 = 1.2, N_{var} = 14, N_{ind} = 21.3, *R* = 0.017, *k* range = 2.5-11, R range = 1-4, window type: Hanning			

Table 3.2: Interatomic distances, Δr, and σ^2 of W-bearing hematite fit to sample BF-11, BF-26 and SYN-$hem_{0.05-1.6}$.

BF-11				BF-26				$SYN\text{-}hem_{1.6}$			
path	N	R [Å]	σ^2	path	N	R [Å]	σ^2	path	N	R [Å]	σ^2
W-O	4	1.822±0.004	0,007	W-O	4	1.823±0.005	0,008	W-O	4	1.845±0.004	0,006
W-O	2	2.100±0.008	0,007	W-O	2	2.09±0.01	0,008	W-O	2	2.087±0.009	0,006
W-Fe	2	3.058±0.006	0,010	W-Fe	2	3.071±0.005	0,010	W-Fe	2	3.059±0.005	0,009
W-Fe	3	3.451±0.006	0,010	W-Fe	3	3.464±0.005	0,010	W-Fe	3	3.452±0.005	0,009
W-O	2	3.382±0.008	0,010	W-O	2	3.38±0.01	0,010	W-O	2	3.487±0.005	0,009
W-O	1	3.382±0.008	0,010	W-O	1	3.38±0.01	0,010	W-O	1	3.487±0.005	0,009
W-O	3	3.473±0.004	0,010	W-O	3	3.480±0.005	0,012	W-O	3	3.587±0.009	0,013
W-Fe	3	3.581±0.004	0,010	W-Fe	3	3.590±0.005	0,012	W-Fe	3	3.605±0.004	0,013
W-Fe	3	3.689±0.008	0,010	W-Fe	3	3.68±0.01	0,012	W-Fe	3	3.676±0.009	0,013
W-O	3	3.769±0.008	0,010	W-O	3	3.670±0.005	0,012	W-O	3	3.685±0.004	0,013
W-Fe	1	3.969±0.008	0,010	W-Fe	1	3.96±0.01	0,012	W-Fe	1	3.885±0.004	0,013
W-O	3	4.119±0.008	0,010	W-O	3	4.11±0.01	0,012	W-O	3	4.107±0.009	0,013
W-O	2	4.271±0.004	0,010	W-O	2	4.279±0.005	0,012	W-O	2	4.366±0.009	0,013
W-O	1	4.272±0.004	0,010	W-O	1	4.279±0.005	0,012	W-O	1	4.294±0.004	0,013
ΔE_0 = 5.2, N_{var} = 14, N_{ind} = 22.5, *R* = 0.015, *k* range = 2.5-11.5, R range = 1-4, window type: Hanning				ΔE_0 =6.6, N_{var} = 15, N_{ind} = 21.3, *R* = 0.019, *k* range = 2.5-11, R range = 1-4, window type: Hanning				ΔE_0 = 8.9, N_{var} = 15, N_{ind} = 23.8, *R* = 0.018, *k* range = 2.5-12, R range = 1-4, window type: Hanning			

Fig. 1: (1 column; 90 mm width)

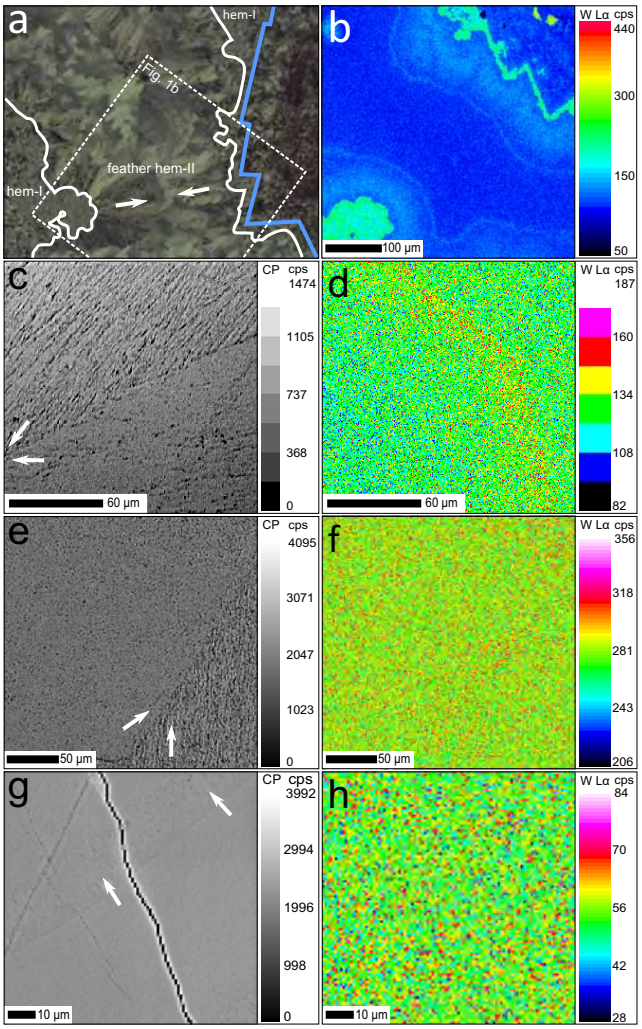

Fig. 2: (2 column; 180 mm width)

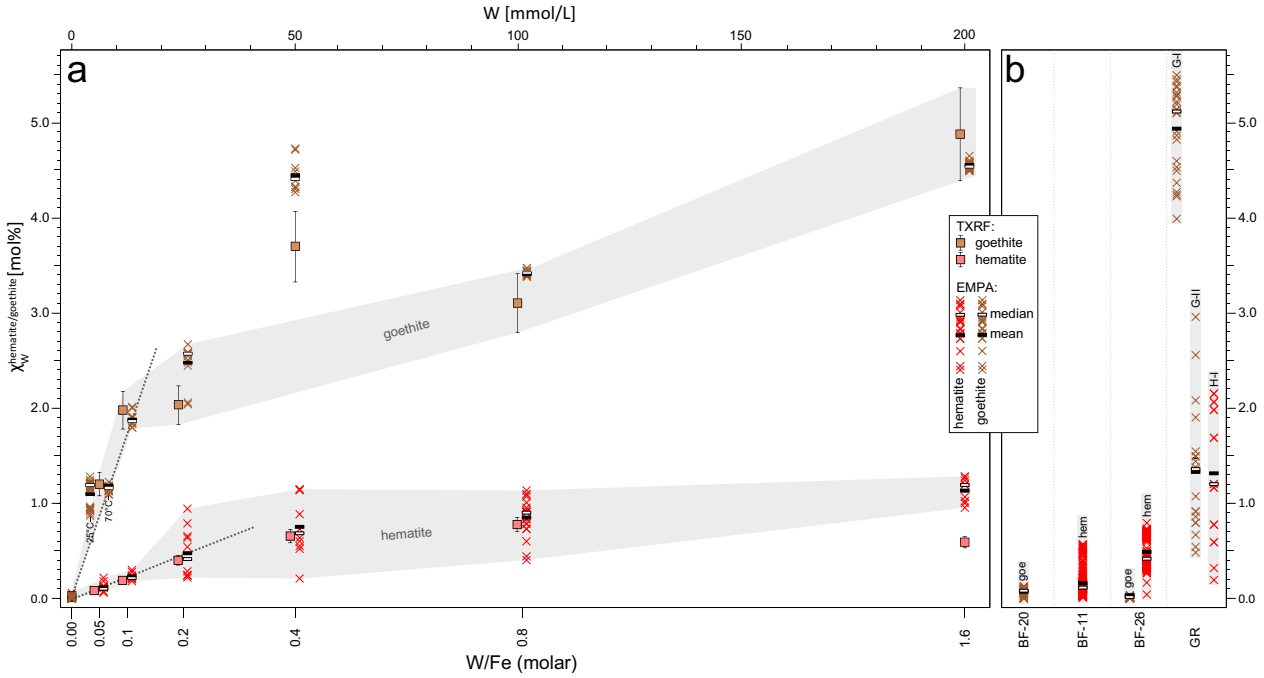

Fig. 3: (1 column; 90 mm width)

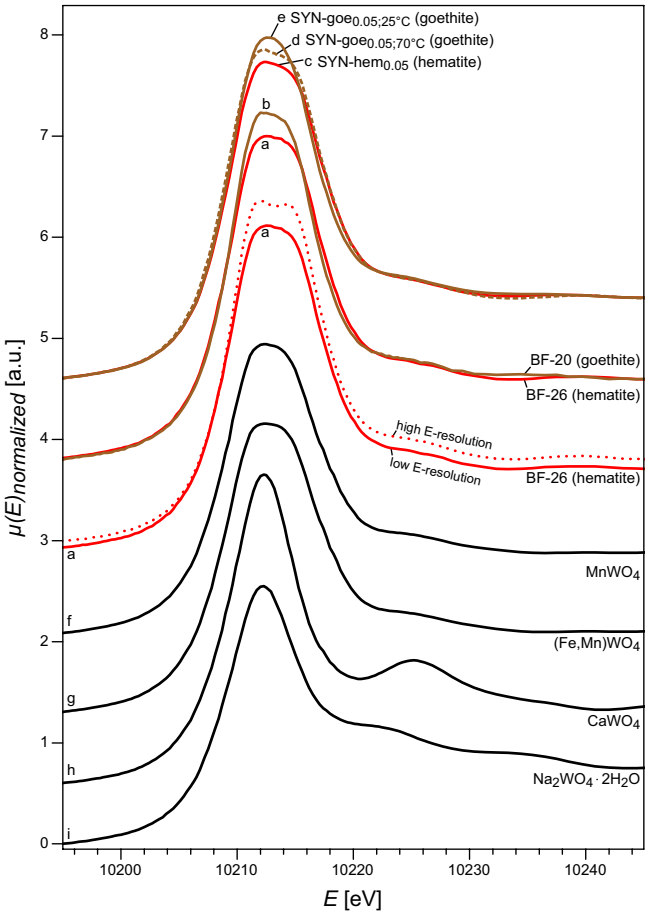

Fig. 4: (1 column; 90 mm width)

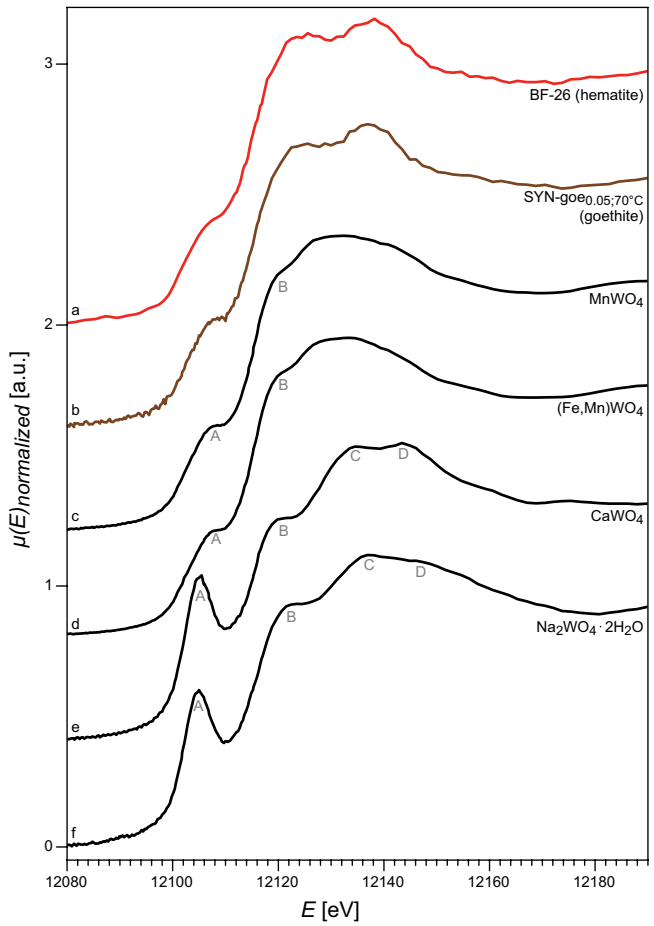

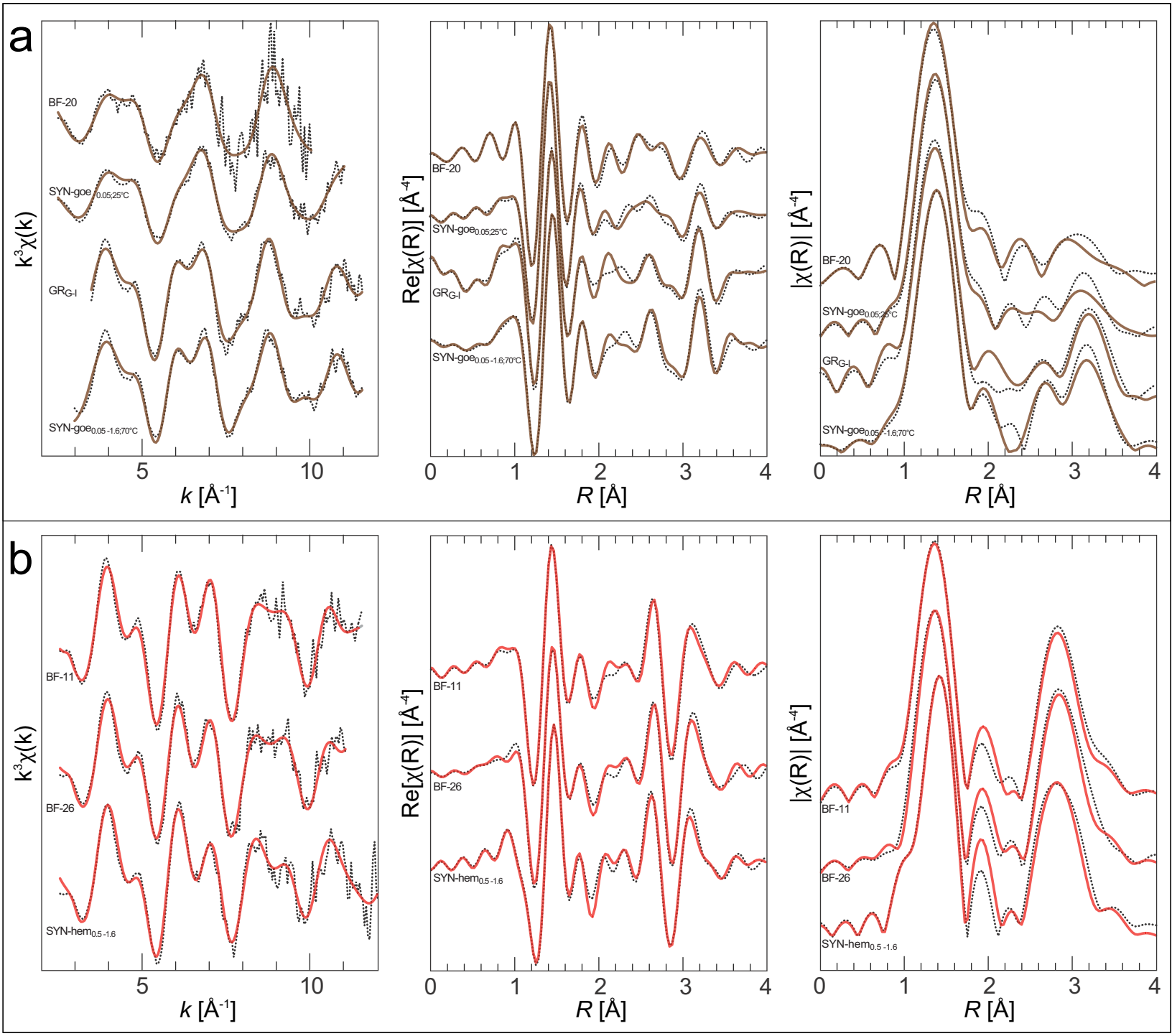
a
BF-20
SYN-goe0.05;25°C
GRG-I
SYN-goe0.05-1.6;70°C
k³χ(k)
k [Å⁻¹]
Re[χ(R)] [Å⁻⁴]
R [Å]
|χ(R)| [Å⁻⁴]
b
BF-11
BF-26
SYN-hem0.5-1.6

Fig. 6: (1 column; 90 mm width)